Photometric and spectroscopic analysis of the interacting supernova 2017dio

UNIVERSITY OF TURKU
Department of Physics and Astronomy

Humina, Christina Photometric and spectroscopic analysis of the interacting supernova 2017dio

Master's thesis, 59 pp.
Physics
October 2023

Core-collapse supernovae (CCSNe) are the bright explosions of massive stars. During the explosion heavy elements are produced by nuclear burning. One of these products is ^{56}Ni that radioactively decays into ^{56}Co. The explosion energy and the produced ^{56}Ni and its product ^{56}Co are what powers the light curves of classical supernovae (SNe).

Stripped envelope (SE) SNe have lost their hydrogen (H) and in some cases, helium (He) envelopes through mass loss at some point in their lives. These SE SNe are known to produce SNe of types IIb (weak H), Ib (He-rich), Ic (He-poor), and Ic-BL (He-poor broad lines). Type IIn SNe, on the other hand, are SNe that interact with circumstellar medium (CSM) around the progenitor. The CSM is thought to be caused by the progenitor's mass loss. The mechanism of the mass loss for these can happen in a variety of ways. All stars have mass loss through stellar winds, but in some cases, it is not enough to produce interaction that would produce a type IIn. The mass loss can also happen because of pair instability pulsations, eruptions, or binary effects. The mass loss can be studied by analysing the observational properties of a SN and understanding the mass loss might shed light on what kind of progenitor produced the SN.

In this thesis, photometric and spectroscopic data of SN 2017dio are analysed. The photometric data are used to study the explosion epoch, light curves, and color curves of SN 2017dio and it is compared with four other SNe. The spectroscopic data are used to verify the classification of SN 2017dio, to study the spectral evolution, and to discuss the possible CSM properties and progenitor scenario.

The findings indicate that SN 2017dio is a SN of type Ic-BL interacting with H-rich CSM. Both spectroscopic and photometric analysis support the theory of the CSM not being close to the explosion site and the calculated mass loss rate $0.04 M_\odot$/year indicates that the progenitor must have experienced massive mass loss periods in the decade before its explosion.

Keywords: supernova, SN 2017dio, interacting supernova

Contents

1 Introduction

Stars, like living things, are born, live out their life and, in the end, die. Low mass stars, like the Sun, go down quietly and fade away after billions of years of living, but more massive stars do not go down as gently. Most massive stars end their lives in violent explosions, sending out their outer layers with a huge amount of energy and they can even, momentarily, become brighter than an entire galaxy. They end their lives as supernovae (SNe).

Supernova (SN) is the last evolutionary stage of most massive stars or white dwarfs that have been accreting matter from a companion. White dwarfs produce type Ia SNe, which are classified by the absence of hydrogen (H) in their spectra and by deep absorption lines of silicon (Si) $\lambda 6150$ Å. Massive stars produce core-collapse SNe (CCSNe), when the fusion of H into heavier elements has gone all the way up to iron (Fe). Fusion reactions usually release energy, that the star needs to support itself against gravity. As fusing Fe would crave energy instead of releasing it, the star has no support and starts to collapse in on itself. These CCSNe produce SNe of type II, Ib, and Ic. Type II SNe show lines of H, while type I SNe do not. The difference between Ib and Ic SNe is the absence of helium (He) in the spectra; Ic SN lacks He lines and in case the absorption features are broad, the SN is called a Ic broad line (Ic-BL). [1]

Furthermore, type II SNe can be subcategorized into different types, depending on their spectral and photometric properties. Type IIb SNe start with H in their spectra but evolve to look like a Ib (H-poor) at later times. On top of all these, we have the interacting SNe, that are called type IIn, "n" for narrow lines. Interacting SNe are more of a feature of the SN and does not tell us anything about the underlying SN type. When the ejecta from the SN explosion hits the circumstellar material around the SN, it may lead to periods of enhanced radiation and peculiarities in the spectra. [1]

In this thesis, a type Ic SN interacting with H-rich CSM is studied, so the focus of this introduction will be on H-poor stripped-envelope (SE) SNe, that are known to produce type Ic SNe (and Ib), and on interacting SNe and their properties.

1.1   Hydrogen-poor stripped-envelope SNe

Stripped-envelope SN comes from progenitors that have lost most of their H and part of their He envelopes. The stripping of these envelopes happens in massive stars due to different types of mass loss. The mass loss could be due to wind [2], eruptions, pair instability pulsations [3] or due to binarity [4]. [5][6]

The light curves of SE SNe resemble those of type Ia. When the SN explodes, a huge amount of energy is suddenly released. Before the first electromagnetic emission emerges, a shock wave (SW) propagates through the envelopes of the star. The SW heats and accelerates the matter, giving thermal and mechanical energy to layers of the envelope. When the shock passes, the gas becomes radiation-dominated. After the SW has arrived at regions where photons can escape, the SN produces its first electromagnetic emissions. This is called the "shock breakout". A few hours after the shock breakout, the effective temperature and the bolometric luminosity rise and reach their peaks. Due to the high temperature, the emission is mostly in the UV/X-ray. [7]

The breakout is followed by an expansion, which cools the outermost layers and increases the photospheric radius. Both the bolometric luminosity and the effective temperature decrease, leading to the emission peak shifting to longer wavelengths. Thus, the peak luminosity is reached later in redder bands. [7]

During the explosion, nuclear burning takes place transforming some of the ejecta matter into heavier elements. One of these products is ^{56}Ni that decays into ^{56}Co. The light curves of type I SNe are usually powered by the explosion energy and the radioactive decay of ^{56}Ni with a half-life of 6.1 days and in late times the decay of

^{56}Co with a half-life of 77.3 days [8].

During the first months, the spectra are dominated by absorption features due to atomic species in the outer ejecta. With time, the ejecta become more transparent and the inner regions are progressively exposed. [7]

1.2   Interacting SNe

Interacting SNe are SNe, whose ejecta interact with the CSM. In principle, every SN interacts with CSM at some point when they expand, but we only want to consider the SNe that show enhanced radiation and spectral peculiarities. [6]

All stars lose mass in the form of stellar winds. If the mass loss is weak the interaction is negligible. Other forms of mass loss can include pulsations, eruptions, and mass transfer in binary stars. These may lead to an enhanced density of the CSM that can lead to many peculiarities in the photometric and spectroscopic characteristics. The structure of the CSM may be quite complicated, it can be uniform or clumpy, and it might be asymmetric. When observing type IIn SNe, it is not the explosion itself that is visible, but the product of the interaction. How the interaction is displayed depends on the density and the velocity of the CSM. If the density is small, the interaction may become visible only after the SN has become faint. If the CSM near the SN is dense, the interaction can dominate over the SN emission and little can be said of the underlying SN type. [6]

Interaction gives rise to many peculiar spectral features; we get the narrow emission line components from the photoionized undisturbed CSM, intermediate emission line component from the shocked CSM, broad emission line components from shocked and/or undisturbed photoionized ejecta, and lastly continuum from shocked ejecta and/or CSM clumps. The velocity of the narrow component approximates the wind velocity, the intermediate approximates the shock velocity, and the broad component the ejecta velocity. [6]

In the light curve, interaction can be seen as a slow luminosity evolution, delayed onsets, multi-peaks, and excess in infra-red due to dust formation or pre-existing dust [9]. The shape of the light curve depends on the interaction and both light curve and spectra may change type depending on when they are observed. [6]

1.3 Previous work

SN 2017dio is a type Ic supernova that evolves into a type IIn. It is one of the first observed of its kind and studying it can shed light on the last moments of the progenitor's life, mass loss, and stellar evolution as a whole. One paper has been done so far on SN 2017dio by Kuncarayakti *et al.* (2018). In the paper, they present an analysis of the first 100 days. The main findings were that the early spectrum of SN 2017dio is similar to those of SNe of type Ic, with a CSM component. The spectra, as well as the light curve, show that the CSM interaction became dominant after the discovery and that the mass loss mechanism is possibly eruptions or binary interaction [10]. SN 2017dio is also one of the SNe studied in Thévenot *at al.* (2021), where it is reported to have late-time mid-infrared (MIR) detections [11]. This thesis aims to make a deeper analysis of the same object, including data from late times, and confirming the results in Kuncarayakti *et al.* (2018).

2 Observations and data reduction

2.1 Detection

SN 2017dio was discovered on 26th of April 2017 (modified Julian date (MJD) =57869) by Asteroid Terrestrial-impact Last Alert System (ATLAS) [12] at an apparent magnitude of 18.29 in cyan band. The discovery was reported by ATLAS_bot1. The last non-detection was on 29th of March 2017 (MJD=57841) [13]. With the help of ATLAS forced photometry [12][14][15] , new non-detection and

detection dates could be determined. In forced photometry, a point-spread-function (PSF) fit is forced to the wanted coordinates. The ATLAS forced photometry has only been available from 2021. Using the data obtained with ATLAS forced photometry, stacking the results per day, and using 3σ as the limit, I found the last non-detection to be on 17th of April 2017 (MJD=57860.39) at a magnitude limit of 20.87 and the first detection on 20th of April 2017 (MJD=57863.51) with an apparent magnitude of 19.04, both in orange band. The mid-point between these dates is determined as the explosion epoch on (MJD=57861.95 $\pm$ 2) approximately 19th of April 2017. Before, no explosion date has been determined for SN 2017dio. The finding chart of SN 2017dio was created with Sloan Digital Sky Survey (SDSS) data release (DR) 14 finding chart tool and is shown in Figure 1 [16].

2.2 Photometry

SN 2017dio was observed photometrically for $\sim$500 days in optical bands and for seven epochs in near-infrared (NIR) with various facilities. Most of the optical observations were carried out by ATLAS in orange-band (some in cyan) and by Liverpool telescope (LT) [17] using the instrument IO:O in $uBgVriz$-bands. The Nordic Optical Telescope (NOT) provided data in $uBgVriz$-bands using the instrument ALFOSC as well as all of the seven epochs in NIR (JHK-bands) using NOTCam. Measurements in V-band were also obtained by Catalina Sky Survey (CSS) [18]. Two data points are from Las Cumbres Observatory (LCOGT) [19] in $griz$-bands.

ATLAS data were obtained from ATLAS forced photometry. The stars used for the photometric calibration are from the ATLAS Refcat2. For LT, I did the photometric measurements with The AUTOmated Photometry Of Transients (Autophot) [20], an automated pipeline producing photometry. For all the $ugriz$-data that I used Autophot on, PSF-photometry – where a PSF function is fit on the light source – was used and the calibration was done with SDSS catalogue [16]. BV-

Figure 1. Finding chart of SN 2017dio, created using the SDSS DR14 finding chart tool. The image used was taken before the explosion of SN 2017dio, so the host galaxy of SN 2017dio is visible in the middle of the image.

bands were calibrated with the AAVSO Photometric All-Sky Survey (APASS) [21]. I also used Autophot for some of the NOT optical photometry and three epochs of NIR photometry. For NIR, Two Micron All-Sky Survey (2MASS) catalogue [22] was used. I did the photometric measurements for NOT data in B- and V-band (and some in $ugrizJHK$) with Graphical Astronomy and Image Analysis Tool (GAIA) [23] with aperture photometry, which will be discussed more in Section 3.3.2. I used SDSS and 2MASS catalogues to calibrate the optical bands and NIR-bands, respec-

tively. The photometric data of *uBgVriz*-bands can be seen in Tables X, XI, and XII in Appendix A. The photometric data from ATLAS is in Table XIII and NIR in Table XIV, also in Appendix A. The data in the tables have not been reddening corrected. *ugcroiz*-bands are in AB system and *BVJHK*-bands in Vega system.

2.3 Spectroscopy

Optical slit-spectroscopy was taken using the instrument EFOSC2 at the European Southern Observatory New Technology Telescope (ESO-NTT), ALFOSC at the NOT, and SPRAT at the LT. ALFOSC spectra were taken with grism #4, which covers the wavelength range 3200-9600 Å and has a resolution of 16.2 Å [24]. The spectra taken with EFOSC2 are a composition of two spectra taken with different grism. One grism, #11 with resolution 15.8 Å, covers the 3380-7520 Å range and the other, #16 with resolution 16 Å, covers 6015-10320 Å [25]. SPRAT uses a grism that covers the wavelengths 4000-8000 Å with a resolution of 18 Å [26].

Most of the spectra were published by Kuncarayakti *et al.* (2018) and are available on the website wiserep (www.wiserep.org), where they are already reduced, wavelength and flux calibrated (not the case for LT spectra).

The spectra from 2017-12-01, 2018-01-13, and 2018-02-15 have not been published yet. They were taken with the NOT as a part of the Nordic-optical-telescope Un-biased Transient Survey (NUTS2). The two last epochs were reduced, wavelength and flux calibrated by the collaboration, but the 2017-12-01 spectrum was not. I subtracted the bias and flatfield corrected the 2017-12-01 spectrum before wavelength and flux calibrating it with IRAF [27]. The problem when reducing the spectrum was that no standard star was observed on the night of observation and the flats from the same night were unusable. I used flats and standard star GD 71 from the night of 2017-12-06 instead.

Table I. Spectroscopy table including dates in UT and MJD as well as the phase in days from explosion, grism used and the range and resolution of the grism. LT+SPRAT only has one grism, so no number is given.

Date (UT)	Telescope+Instrument	Phase (d)	MJD	Grism	$\Delta\lambda$ (Å)	Range (Å)
2017-04-30	ESO-NTT+EFOSC2-NTT	11	57874	13	21.2	3685-9315
2017-05-01	ESO-NTT+EFOSC2-NTT	12	57874	11	15.8	3380-7520
2017-05-01	ESO-NTT+EFOSC2-NTT	12	57874	16	16	6015-10320
2017-05-02	NOT+ALFOSC	13	57875	4	16.2	3200-9600
2017-05-13	LT+SPRAT	24	57886		18	4000-8000
2017-05-14	NOT+ALFOSC	25	57887	4	16.2	3200-9600
2017-05-23	NOT+ALFOSC	34	57896	4	16.2	3200-9600
2017-06-02	ESO-NTT+EFOSC2-NTT	44	57906	11	15.8	3380-7520
2017-06-02	ESO-NTT+EFOSC2-NTT	44	57906	16	16	6015-10320
2017-06-19	NOT+ALFOSC	61	57923	4	16.2	3200-9600
2017-07-18	NOT+ALFOSC	90	57952	4	16.2	3200-9600
2017-12-01	NOT+ALFOSC	226	58088	4	16.2	3200-9600
2018-01-13	NOT+ALFOSC	269	58131	4	16.2	3200-9600
2018-02-15	NOT+ALFOSC	302	58164	4	16.2	3200-9600

3 Methods

3.1 Redshift and dereddening of the spectra

In this work, I have corrected the spectra of SN 2017dio for reddening and redshift. The dereddening of the spectra was done with IRAF using the task deredden. For the task, the extinction parameter A_V (or $E(B - V)$) needs to be known. The value for A_V in Milky Way is from NASA/IPAC infrared science archive (https://irsa.ipac.caltech.edu/applications/DUST) and has the value $A_V = 0.0824$ (Schlafly & Finkbeiner (2011)) [28]. R_V value is assumed to be 3.1, which is typical for the Milky Way [29].

The redshift was calculated with

$$z = \frac{\lambda_{\mathrm{obs}}}{\lambda_{\mathrm{rest}}} - 1 \tag{1}$$

where λ_{obs} is the observed wavelength and λ_{rest} is the rest wavelength of the same line. The redshift in this work was calculated by using the narrow Hα emission line in all the spectra and was confirmed by calculating the redshift from the narrow Hβ emission lines. Some of the spectra appear to have small offsets in the wavelength, so the redshift is calculated as the mean of all the measurements and is $z = 0.036 \pm 0.001$, which is consistent with the reported redshift of SN 2017dio [30]. The error is calculated as the standard deviations of the measurements.

3.2 Hα velocities

I calculated the line velocities by measuring the Lorentzian full width at half maximum (FWHM) of Hα emission lines from redshift-corrected spectra. I used Lorentzian fits for the Hα emission lines, as most of them show Lorentzian wings and are thus better fit with a Lorentzian. I corrected the FWHM for instrumental broadening, which were achieved by measuring the Gaussian FWHM of the sky emission lines using IRAF. A Gaussian fit was used as it provided a better fit for the sky emission lines. I measured the instrumental broadening for four different grisms.

Table II. Measured $\mathrm{FWHM_{sky}}$ for the sky emission lines for each grism used to measure velocities.

Telescope+Instrument	Grism	$\mathrm{FWHM_{sky}}$ (Å)
ESO-NTT+EFOSC2-NTT	13	13.8
ESO-NTT+EFOSC2-NTT	11	13.7
NOT+ALFOSC	4	12.0
LT+SPRAT		10.0

ESO+EFOSC2 #13 and #11, NOT+ALFOSC #4, and for the grism used in LT+SPRAT. The measured values can be seen in Table II. The measured values for the FWHM of the sky emission lines are lower than the spectral resolution for the grism. The errors of the FWHM for the sky emission lines are not taken into account in further measurements.

I used two different programs to measure the Lorentzian FWHM of the Hα: IRAF and Python. The first six spectra were fit with one Lorentzian to measure the FWHM of the narrow component. The spectra that showed broad/intermediate components were fitted with two Lorentzian, to distinguish the narrow component from the broad component. With Python, I first cut the spectra to range from 6300 Å to 6700 Å and then subtracted the continua by fitting a line to the data. The spectra were then normalized by Hα flux.

All FWHM were then corrected for instrumental broadening using

$$\mathrm{FWHM} = \sqrt{\mathrm{FWHM_{obs}}^2 - \mathrm{FWHM_{instr}}^2} \tag{2}$$

where $\mathrm{FWHM_{obs}}$ is the observed FWHM and $\mathrm{FWHM_{instr}}$ is the instrumental broadening. The corrected FWHM is then converted to velocity with

$$v = \frac{\mathrm{FWHM}}{\lambda_{\mathrm{rest}}} \cdot c \tag{3}$$

where λ_{rest} is the rest wavelength of Hα and c the speed of light.

Table III. Table of the Hα velocities. The v_n and v_b velocities were measured by fitting a Lorentzian to the emission line using IRAF and Python. Spectra that were easily fitted with one Lorentzian only has a narrow or a broad component, spectra that needed two Lorentzian to fit have two components. v_n is the velocity for the narrow component and v_b is the velocity for the broad component. *The phase is given in days from explosion.

Date (UT)	MJD	Phase*	v_n	v_b	v_n	v_b
		(d)	IRAF	(km/s)	Python	(km/s)
2017-04-30	57873	11	466 ± 30		457 ± 50	
2017-05-01	57874	12	354 ± 15		371 ± 20	
2017-05-02	57875	13	344 ± 10		363 ± 10	
2017-05-13	57886	24	533 ± 40		537 ± 35	
2017-05-14	57887	25	458 ± 20		423 ± 20	
2017-05-23	57896	34	422 ± 25		435 ± 15	
2017-06-02	57906	44	675 ± 65	9070 ± 1300	634 ± 45	6781 ± 3100
2017-06-19	57923	61	533 ± 10	4395 ± 330	545 ± 45	4609 ± 290
2017-07-18	57952	90	806 ± 60	3168 ± 180	782 ± 80	3190 ± 110
2017-12-01	58088	226		1922 ± 80		2066 ± 25
2018-01-13	58131	269		1322 ± 25		1386 ± 20
2018-02-15	58164	302		1209 ± 10		1277 ± 25

With IRAF, the Lorentzian needs to be fit interactively and all the measurements are quite sensitive to how the continuum is chosen. The Lorentzian was fit five times, choosing the continuum slightly differently each time, and a mean value of the fits was used as the FWHM. The error was calculated as the standard deviation of the fits. As for the errors with Python, I achieved the standard deviations from the fits. The velocities are listed in Table III and the Lorentzian fits I obtained with Python are plotted in Figure 2. The values I achieved from IRAF and Python are always consistent within the errors.
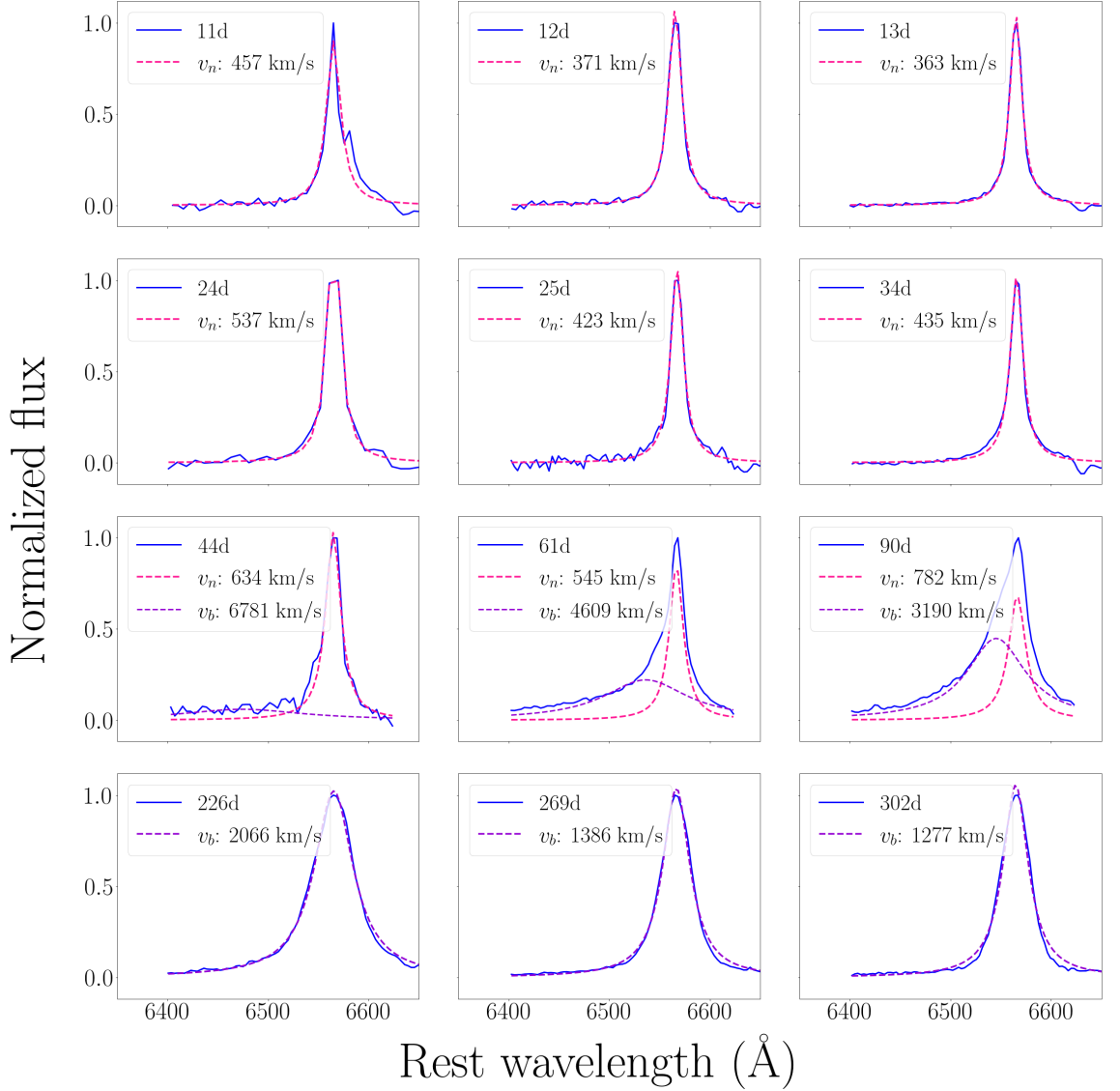
Figure 2. Hα lines at different phases. The phases are shown as days from the explosion in every panel. The continua have been subtracted from the spectra and the flux is normalized. The Lorentzian fits are plotted with a dashed pink line on top of the original feature in blue. The corrected FWHM of the fitted Lorentzian and the velocities are listed in all the spectra. v_b is the velocity of the broad component and v_n is the velocity of the narrow component.

3.3 Photometric measurements

3.3.1 Autophot

Autophot was used to produce photometric measurements of the object. Before running Autophot itself, coordinates for the object need to be defined, the photom-

etry method (PSF or aperture) needs to be chosen as well as the catalogue used to calibrate the zeropoints. After autophot is run, the program will go through the fits-files and ask for some keywords to be able to determine the telescope location, the name for telescope+instrument, pixel scale in arcsec/pixel, gain, readnoise, airmass, and filter from the header. For some of these, autophot is able to find the corresponding keyword from the header, but for example the keyword for readnoise in LT is readnois and that needs to be inserted for autophot to be able to find it from the header. It will also ask one to manually insert all the corresponding filters that are found in the fits-files.

To get all the bands (*uBcVgriz-JHK*), the program must be run multiple times as not one of the catalogues has data for all bands.

3.3.2   GAIA

Calibration for some of the photometry was done with the software GAIA using three different sky survey catalogues: SDSS DR14 was used for *ugriz*-bands, APASS DR10 for *BV*-bands and 2MASS for *JHK*-bands. For *ugriz*-bands, seven field stars were chosen from the science images (same stars in all bands), and their magnitudes were read from the catalogues. Six of the same stars were used for *JHK*-bands as not all the stars had data in *JHK*-bands. For *B*- and *V*-bands, four new field stars were chosen, as none of the previously used field stars had data in *B*- and *V*-band.

GAIA was used to measure aperture photometry on the targets and on the chosen field stars. Zero points, difference in magnitudes measured with GAIA and magnitudes read from catalogues, were calculated for all the chosen field stars. Taking an average of the zero points and subtracting it from the magnitude of SN 2017dio measured with GAIA, gives the calibrated magnitude of SN 2017dio. Color terms are assumed to be zero. The errors for the magnitudes were calculated with the
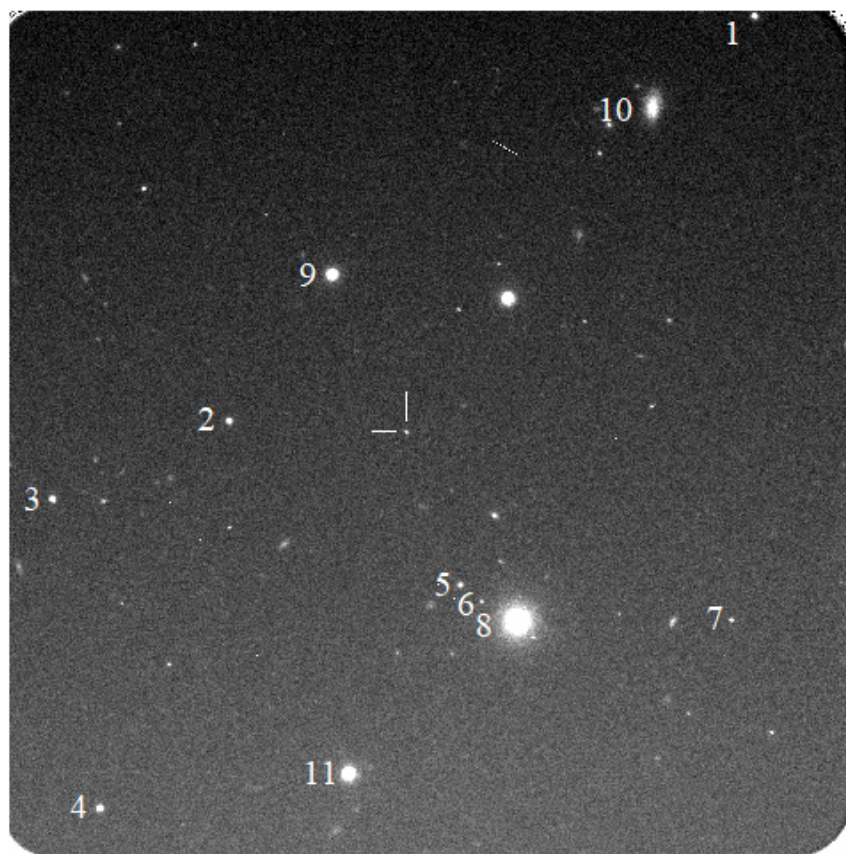
Figure 3. Image taken with the Nordic Optical Telescope on 2018-02-14 in g-band. The field stars used in the calibration of measurements gained with GAIA are marked in the image. The position of SN 2017dio is pointed out with two lines.

standard deviation

$$\sigma = \sqrt{\frac{\sum_{n=1}^{N}(x_n - \bar{x})^2}{N-1}} \tag{4}$$

where x_n is the magnitude of one field star measured with GAIA, $\bar{x}$ is the calculated zero point and N is the number of field stars.

When doing the aperture photometry, the semi-major radius, annulus inner scale and annulus outer scale could be adjusted. It was important to get all the light from the supernovae inside the semi-major axis circle and to adjust the inner and outer annulus to exclude any bright objects or light from other sources, as this part is used to subtract noise from the sky. The semi-major axis was kept the same for the target and all the field stars. The coordinates, names and magnitudes of the used field stars can be seen in Table IV and the locations in Figure 3

Table IV. Table of the field stars used in calibration. SDSS catalogue was used for *ugriz*-bands, APASS for *VB*-bands and 2MASS for *JHK*-bands.

Number	RA	Dec	u	B	g	V	r	i	z	J	H	K
1	174.06922	+18.34964	19.69		17.90		17.08	16.81	16.66	15.83	15.19	15.28
2	174.13953	+18.29780	20.09		18.20		17.48	17.21	17.06	16.28	15.46	15.74
3	174.16330	+18.28780	19.24		18.20		17.82	17.68	17.58	16.66	16.18	16.13
4	174.16330	+18.24844	20.46		17.92		16.71	16.18	15.91	14.78	14.09	14.01
5	174.10869	+18.27707	21.37		18.72		17.26	15.98	15.30	13.97	13.33	13.06
6	174.10558	+18.27488	21.17		20.10		20.01	20.03	20.16			
7	174.07208	+18.27268	21.85		19.56		18.16	17.44	17.04	15.71	15.18	14.93
8	174.100792	+18.272445		13.33		12.70						
9	174.125898	+18.316523		15.92		15.32						
10	174.08295	+18.337988		17.33		16.42						
11	174.123467	+18.252973		15.55		14.67						

3.4 Photometric corrections: Extinction correction and galaxy subtraction

The photometric data gathered in the Appendix A (Tables X-XIV) are the apparent magnitudes of the object in different bands, and they are not corrected for interstellar reddening. Interstellar reddening is a product of the interstellar dust absorbing and scattering blue wavelengths more than red, making objects appear redder than they are. The photometric data used to make the light curves of SN 2017dio are corrected by the extinction values that are listed in Table VI.

Values for most of the extinction correction are from NASA/IPAC Extragalactic Database (NED), except for orange and cyan, which were not available and had to be calculated with the Cardelli extinction law

$$< A(X)/A(V) >= a(x) + b(x)/Rv \tag{5}$$

where $Rv = 3.1$, $A(V)_{\text{SFD}} = 0.0958$ (mag) (SFD = Schlegel *et al.* (1998)), and

$$a(x) = 1+0.17699y-0.50447y^2-0.02427y^3+0.72085y^4+0.01979y^5-0.77530y^6+0.32999y^7 \tag{6}$$

and

$$b(x) = 1.41338y+2.28305y^2+1.07233y^3-5.38434y^4-0.62251y^5+5.30260y^6-2.09002y^7 \tag{7}$$

where $y = (x - 1.82)$ and x is the effective wavelength of the filter. [31] The effective wavelengths for ATLAS cyan- and orange-band are taken from the SVO Filter Profile Service [32].

As the spectra show no sign of Na I D absorption features, which usually correlates with the amount of dust along the line of sight, we can assume that the reddening from the host galaxy is negligible [33]. On top of needing to be corrected for interstellar reddening, SN 2017dio is not resolvable from its host galaxy. This means that the photometry of SN 2017dio is affected by emission from the host

Table V. The name of the galaxy, its coordinates, and apparent magnitudes in ugriz-bands.

Name	RA	Dec	u	g	r	i	z
SDSS J113627.76+181747.3	174.11569	+18.29649	23.36	21.12	20.67	20.55	20.12

galaxy. This is not a problem when the SN is bright, but at late times the light curve is significantly affected by it. Galaxy subtraction was done with

$$m = -2.5\log(10^{-0.4m_{\mathrm{SN}}} - 10^{-0.4m_{\mathrm{g}}}) \tag{8}$$

where m_{SN} is the apparent magnitude of the supernova and m_{g} is the magnitude of the galaxy in the same band. The galaxy subtraction was done in $ugriz$-bands, as those were the only magnitudes that could be found for the host galaxy. The apparent magnitudes of the galaxy are taken from SDSS DR18 [34] and are listed in Table V. There might be some uncertainties in the measurements as the aperture size of PSF fitting used in photometric measurements done of SN 2017dio might not be the same as the aperture size of PSF used in SDSS.

3.5 Absolute magnitude

As mentioned, the data gathered are in apparent magnitude, which tells how bright the object appears to an observer. However, if we want to compare the brightness of the object with other objects, it is important to know how bright their absolute magnitude – brightness from the same distance – is. The absolute magnitude is calculated with the distance modulus

$$m_\lambda - M_\lambda = 5\log(D_{\mathrm{lum}}) - A_\lambda \tag{9}$$

where m_λ is the apparent magnitude, M_λ is the absolute magnitude, A_λ is the extinction, all at a certain wavelength and the luminosity distance

$$D_{\mathrm{lum}} = \frac{2c}{H_0}(1 - \sqrt{\frac{1}{1+z}})(1+z) \tag{10}$$

Table VI. The extinctions values listed by band.

Band	A_λ	ref
u	0.164	[35]
B	0.138	[28]
g	0.121	[35]
c	0.103	
V	0.106	[28]
r	0.088	[35]
o	0.077	
i	0.067	[35]
z	0.047	[35]
J	0.029	[28]
H	0.018	[28]
K	0.012	[28]

where c is the speed of light, $H_0 = 70\text{km/s/Mpc}$ and z is the redshift of the object, in this case, $z = 0.037$. The achieved D_lum for SN 2017dio is ≈ 160 Mpc and the distance modulus is 36 mag.

3.6 Bolometric light curve and blackbody parameters

Superbol [36] was used to produce the bolometric light curve and to calculate the blackbody temperature and blackbody radius of SN 2017dio. Superbol is a program that calculates the pseudobolometric light curves by integrating flux over observed filters. It converts the observed magnitudes to fluxes and uses trapezoidal integration to get the luminosity, where the flux is assumed zero outside the observed band. Flux errors and bandwidths are used to get the luminosity error. It also constructs a spectral energy distribution (SED), that is fitted with a blackbody and the tem-

perature and radius gained from it are also used to calculate the luminosity using Stefan-Boltzmann law

$$L = 4\pi R^2 \sigma T^4 \tag{11}$$

where L is the luminosity of the object, R is the radius of the object, σ is the Stefan-Boltzmann constant and T is the temperature in K. The UV luminosity is integrated bluewards of the bluest band and NIR redwards from the reddest band. [36]

The bolometric light curve for SN 2017dio is built up with $uBgVroizJHK$-bands. When building up the bolometic light curve, the different light curves are fitted with polynomials so they can be extrapolated if needed. r-band was used as a reference since it had the most data points.

For $griz$-bands, a 4th order polynomial was fitted and as they had good coverage, no extrapolation was needed. For V- and o-band, a 4th order polynomial was also fitted, but they had to be extrapolated at late times. An average of polynomial fit and consistent color fit was used. Because of the lack of data, a 2nd order polynomial was fitted to $uBJHK$-bands and similarly, an average extrapolation was done on them both at early and late times.

The light curves are corrected for both time-dilation using redshift and for reddening. All of the given data need to be in their default photometric system and the flux and wavelength are converted to rest-frame.

The last steps are to apply UV absorption below 3000Å and give initial guesses for the temperature and radius. When the bolometric light curve constructed for this work was done, $T = 10000$K and $r = 1.0 \cdot 10^{15}$cm were used.

The bolometric light curve is a combination of the integrated flux, UV-correction and NIR extrapolation. The bolometric light curve built with Superbol can be seen in Figure 4 and the fitted blackbody temperatures and blackbody radius in Figure 5. For comparison, a blackbody function was fitted as spectral radiance of a body

for wavelength λ at absolute temperature T as

$$B_\lambda(\lambda, T) = \frac{2hc^2}{\lambda^5} \frac{1}{e^{hc/(\lambda k_B T)} - 1} \tag{12}$$

where k_{B} is the Boltzmann constant and h is the Planck constant, on top of the five first epochs of spectra to see if the temperature gained with Superbol provided good values. The temperatures achieved for the earliest epochs are underestimated as the fits should be above the spectra due to absorption lines eating the flux. The fitted blackbody on spectra are plotted in Figure 6 and the corresponding temperatures are plotted in Figure 5 with colored markers.
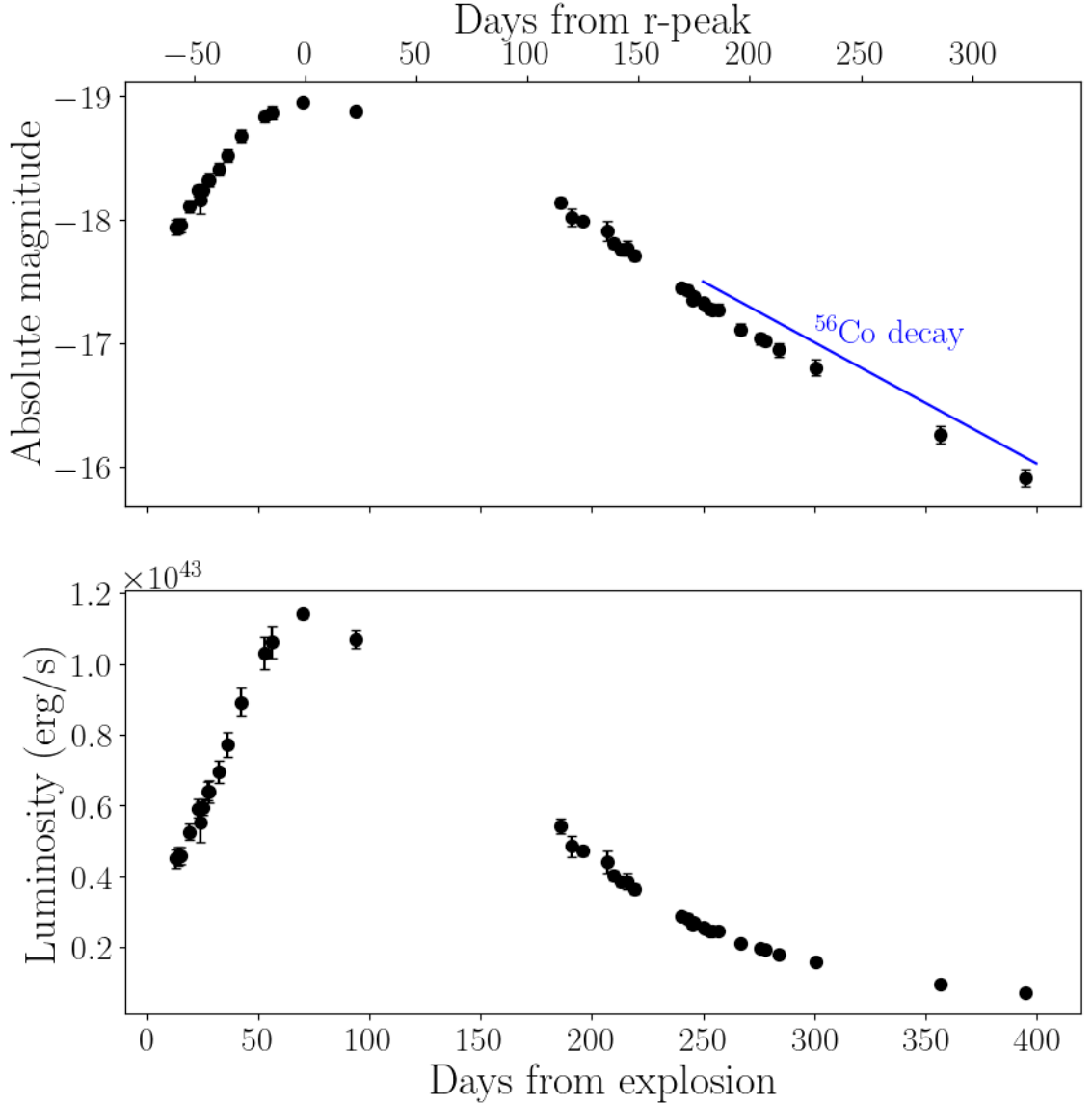
Figure 4. Bolometric light curve of SN 2017dio achieved with Superbol. In the upper panel, the light curve is plotted in absolute magnitude and in the lower panel in luminosity. The upper x-axis tells the epoch in days from r-peak and the lower x-axis in days from explosion. The blue line in the first panel follows the ^{56}Co radioactive decay of 0.0098 mag/day.

3.7 Gaussian process

Gaussian process regression (GPR) was used to find the peak times and peak magnitudes of the light curves. Gaussian process (GP) is good for fitting as it does not need a physical or analytical model to fit the data. GP uses multivariate Gaussian distribution, which is a generalization of the one-dimensional distribution to higher
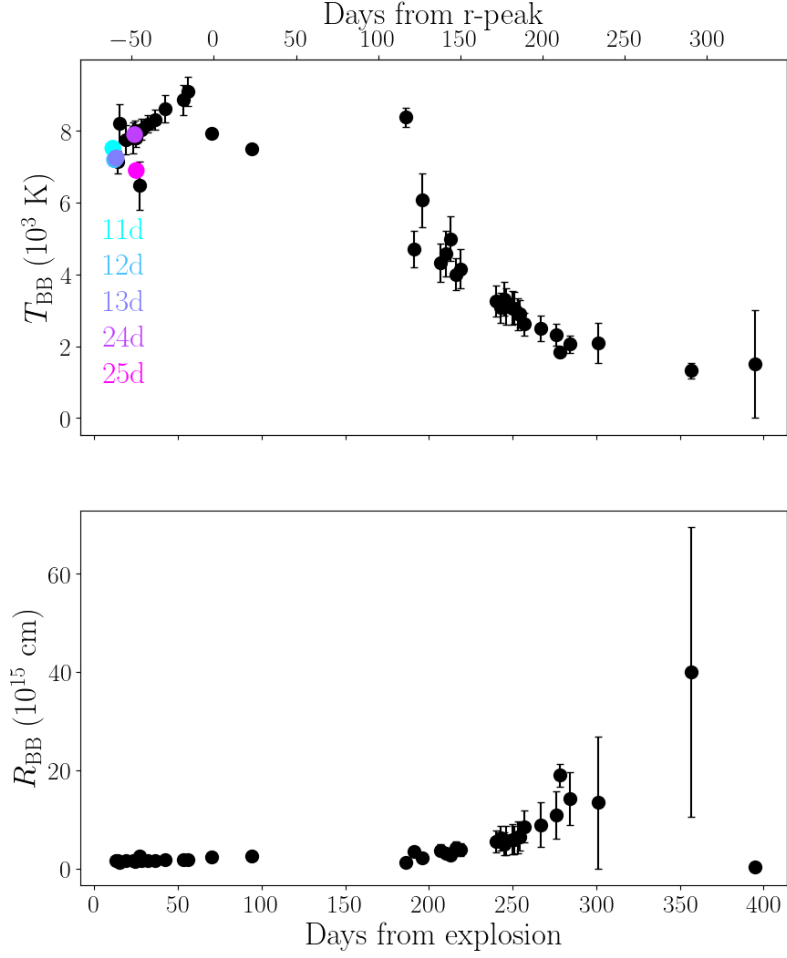
Figure 5. The blackbody temperature obtained from Superbol is plotted in the upper panel and the blackbody radius obtained with Superbol is plotted in the lower panel. The colored markers in the temperature plot correspond to the temperature achieved by fitting a blackbody to the spectra plotted in the Figure 6. The epochs of the spectra are shown in the panel.

dimensions.[37] For a given set of data points, there is an infinite number of possible functions that fit the data. In GPR, the GP considers all the functions and adds a probability to them to see which are more probable. This naturally gives uncertainties on the data points. GP is entirely specified by its mean value function $\mu(\mathbf{x})$, which is the mean of the functions, and the covariance function k$(\mathbf{x},\mathbf{x}')$. The covariance function is in this case defined by kernels and kernels control what kind of functions are fitted to the data. A kernel is a function that measures the similarity of two inputs $\mathbf{x}$ and $\mathbf{x}'$. GP then evaluates functions that produce similar outputs
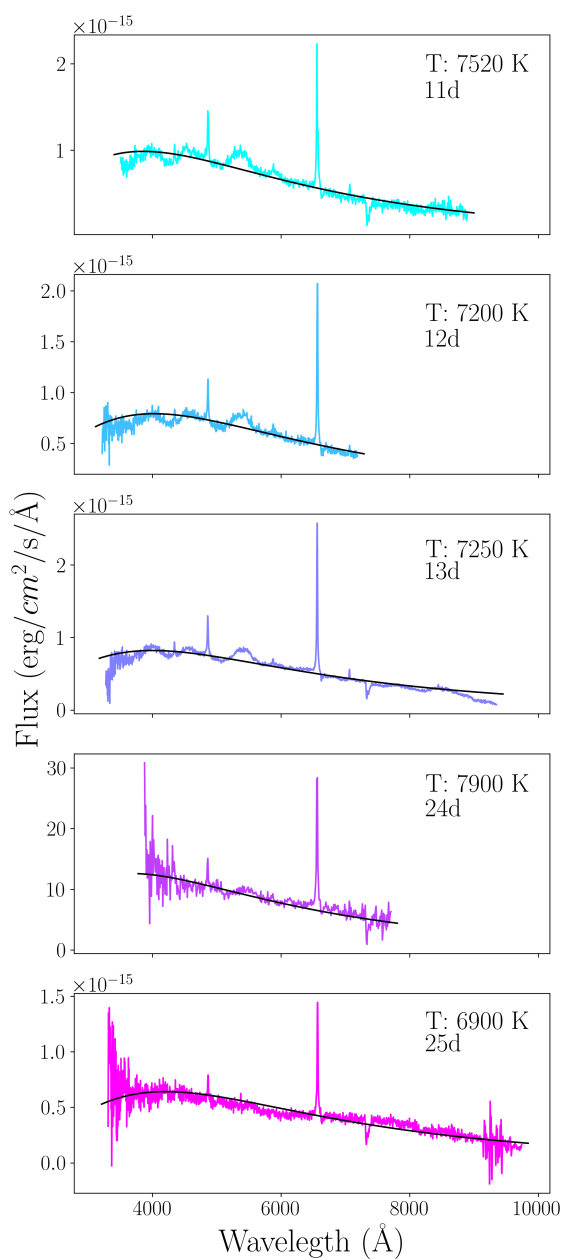
Figure 6. A blackbody function fitted on top of the five first epochs of spectra. The temperatures achieved with the fits as well as the epochs of the spectra are listed in each panel.

for **x'** determined to be similar by the kernel. [38]

When fitting light curves, the functions have the independent variable time t and the dependent variable observed magnitude m. The GP model approximated

of m and t can be written as the probability distribution function

$$p(m|t) = N(\mu(t), K) \tag{13}$$

where $\mu(t)$ is the mean function describing how the value of m varies as a function of t, and K is the covariance function. As mentioned, kernels control what kind of functions are fitted, so when choosing the kernel, it is important to choose a kernel that follows the characteristics expected to be seen in the approximated function. For SN light curves, squared-exponential-kernel and Matérn3/2-kernel are usually used. [37]

In this work, Matérn3/2-kernel was used. It is defined as

$$k(x, x') = \sigma^2 \cdot (1 + \frac{\sqrt{3(x - x')^2}}{l} \cdot \exp(\frac{-\sqrt{3(x - x')^2}}{l})) \tag{14}$$

where the variance σ^2 and length scale l are hyperparameters which control the kernel. The variance defines how much the fitted functions are able to vary from the mean function and the length scale how smooth the resulting functions can be. Figure 7 shows the heatmap of Matérn3/2-kernel that is, which values x and x' the kernel thinks are similar, and Figure 8 shows a sample of what kind of functions GP draws with the kernel.

GP does have a problem with fitting if there is a big gap in the data, so when the peak times and magnitudes were estimated, only the data before the gap in the light curves were fitted. The error in peak magnitude is achieved with the standard deviation provided by GP. The errors in peak times are taken as the time between the estimated peak and the observed peak magnitude times and the error in the explosion date.
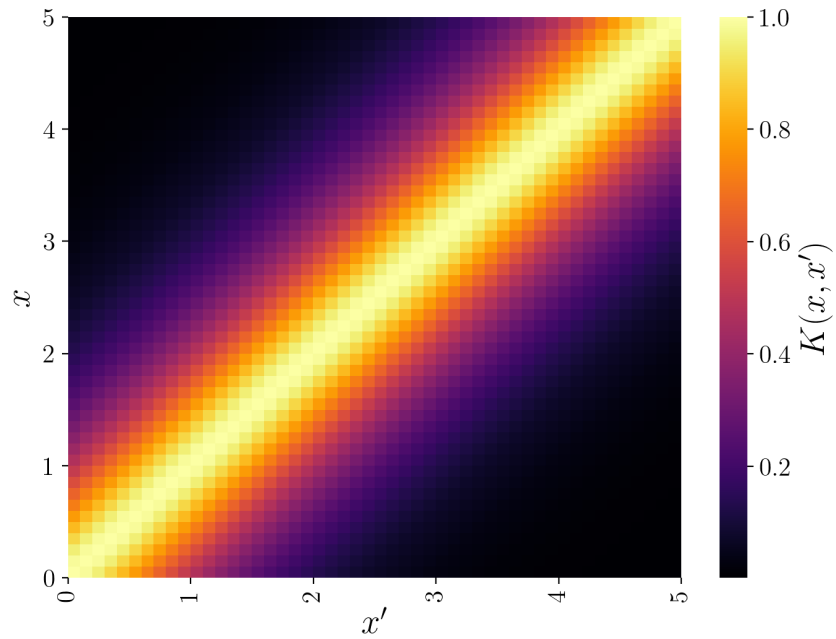
Figure 7. Heatmap of Matérn3/2-kernel showing the similarity between x and x' according to the kernel. In this heatmap, lengthscale l and the variance σ are both 1.
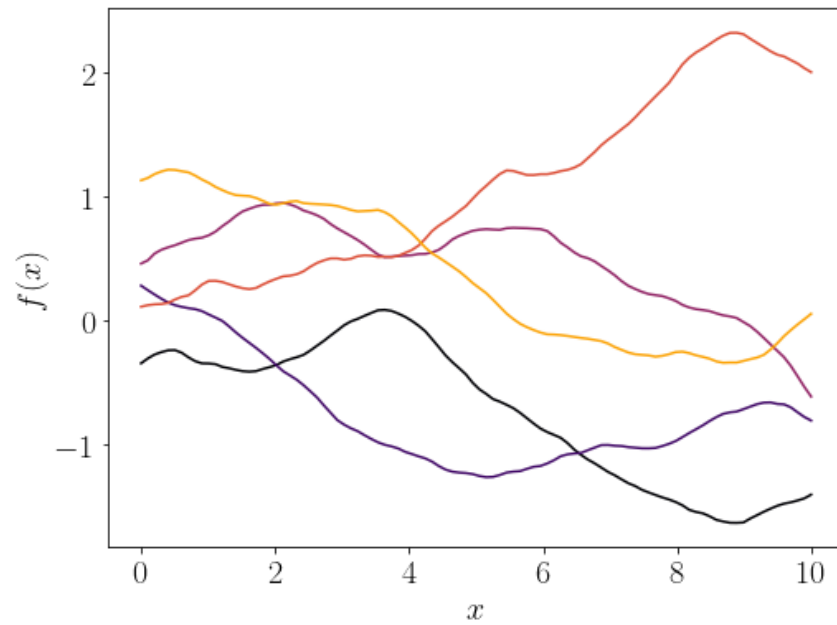

Figure 8. Sample of functions that the Gaussian process makes using the Matérn3/2-kernel. This is prior to any data.
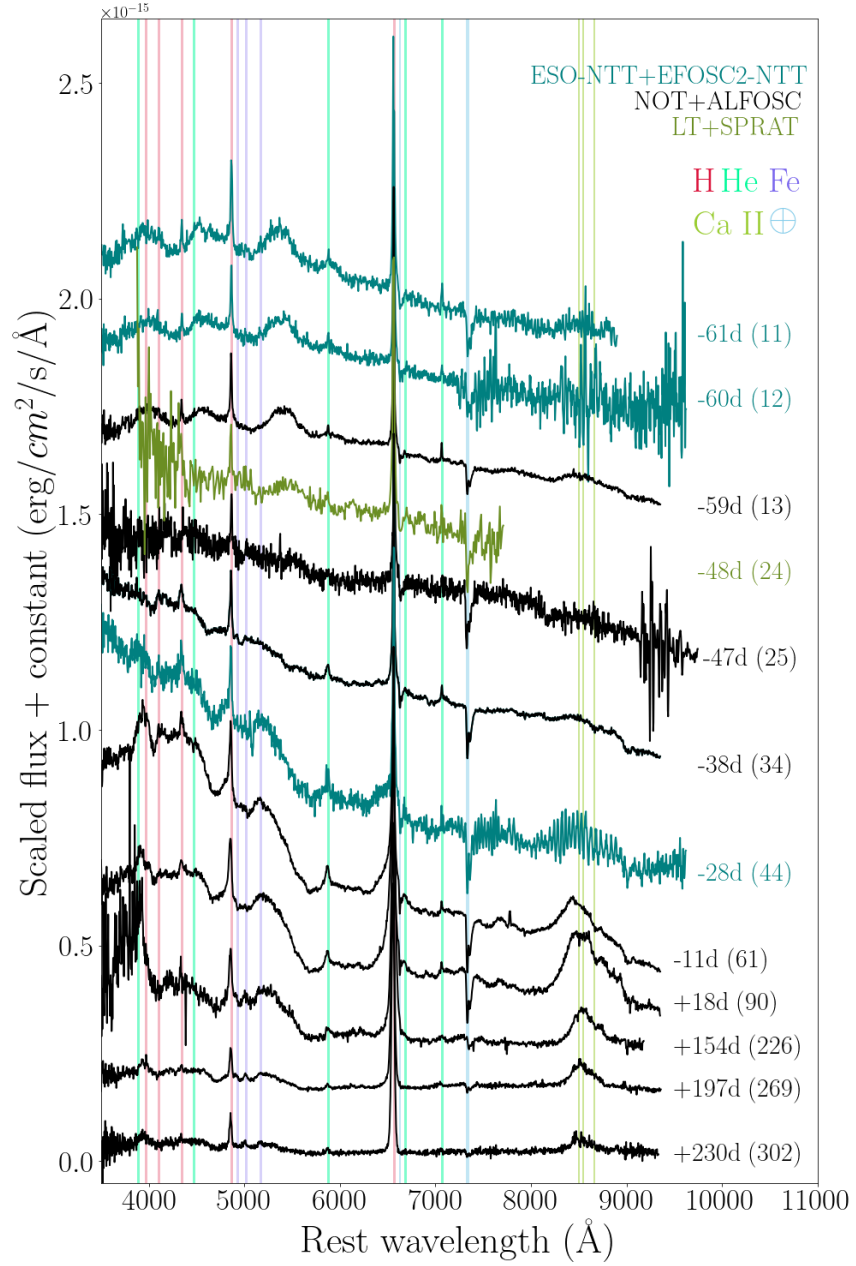
Figure 9. Spectral sequence of SN 2017dio. The epochs of the spectra are in days from r-peak and in days from the explosion in parenthesis. The spectra in teal color are taken with the ESO-NTT+EFOSC2-NTT, the black spectra with the NOT+ALFOSC, and the green spectrum with the LT+SPRAT. The spectra are redshift corrected and the x-axis is in rest wavelength. All the spectra are scaled to have similar Hα strength and are shifted. For presentation, the spectra are cut to start from 3500 Å. The hydrogen lines are marked with red lines, helium with green, iron with violet, calcium II with yellow, and the telluric lines with blue.

4 Results and discussion

4.1 Spectral evolution

The spectral evolution of SN 2017dio is shown in Figure 9. In the three first spectra, 11, 12, and 13 days from the explosion, we can see spectra that have broad absorption lines and narrow hydrogen emission lines, where Hα (λ6563) and Hβ (λ4861) are strongest. Weak, narrow He emission lines can also be seen at wavelengths $\lambda\lambda$5876, 7065. Broad absorption lines and no broad H or broad He absorption/emission lines indicate that the spectra belong to a type Ic-BL supernova, that has narrow emission lines superimposed.

At around 25 days from the explosion and 47 days before r-peak, the spectra evolve and become dominated by the interaction and the broad absorption features can no longer be distinguished. At this time, the spectrum is quite featureless, and only narrow H emission lines can be recognized from the spectrum.

Later on, the spectra evolve a bump in the bluer parts, which could be broad blends of Fe as suspected for SN 2002ic [39]. If this is the case, then they could have originated from the cool shell in the reverse shocked region or from dense CSM clouds.[39]

In the redder parts a broad emission line of Ca II NIR-triplet $\lambda\lambda\lambda$8498, 8542, 8662 shows up. This line might be a blend of O I λ8446 and the Ca II NIR-triplet. This Ca II NIR-triplet is first well distinguished in the spectrum 61 days from the explosion and 11 days before r-peak. The triplet grows stronger after the r-peak, but in the last three spectra, it is weakening again. The bump seen in the bluer parts starts to weaken after r-peak. Both of these might be a product of the interaction, which would suggest that the interaction is strongest during/around the light curve peak.

The evolution of the Hα profile can be seen in Figure 10. The profile starts as a
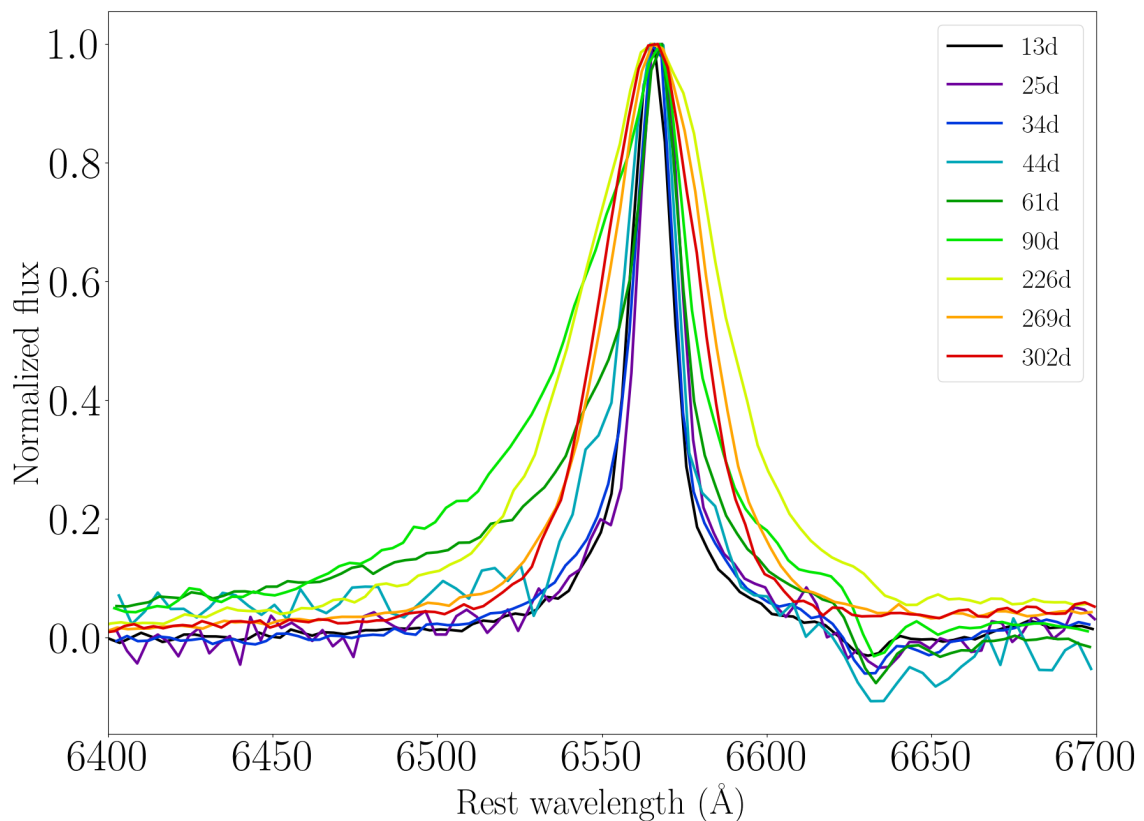
Figure 10. Evolution of the Hα profile between 13 and 302 days from the explosion. The spectra have been normalized to have the Hα flux equal to one and are shifted to have the peak in the same place. For clarity, spectra with similar epochs have been omitted. The spectra taken 44 days from the explosion has different spectral resolution compared with the others, so the comparison might be affected by it.

narrow emission line with Lorentzian wings most likely from electron scattering due to the SN shock being able to ionize the surrounding CSM, making the optical depth substantial to electron scattering. This can happen in a SN with dense CSM and the broad wings on narrow lines are an observed signature of electron scattering. [40] Up until 34 days, the Hα does not evolve much, but after 34 days, the emission lines get broader. The broadening emission lines and the rise of Hα luminosity indicate that the interaction is indeed getting stronger, which is consistent with the theory of the "bump" and Ca II NIR-triplet showing the strength of the interaction. The evolution of the Hα luminosity is plotted in Figure 11.

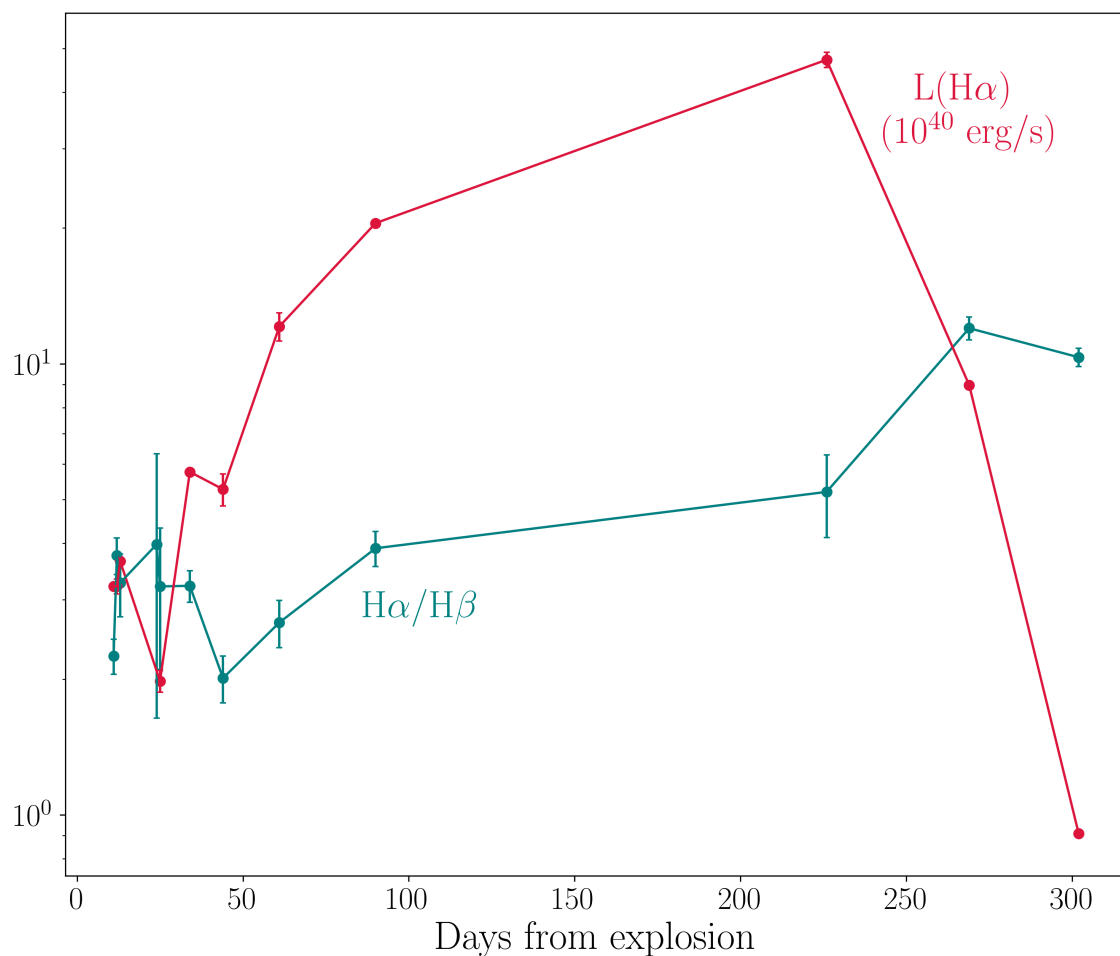The broad emission is strongly asymmetric and shows suppression of the red

Figure 11. The evolution of Hα and Hβ ratios plotted in teal and the Hα luminosity evolution plotted in red. The y-axis has a logarithmic scale and the x-axis tells the days from the explosion. The Hα luminosity has the units 10^{40} erg/s.

wing up until 90 days. As there is a telluric absorption line redward after Hα, it is possible that the telluric line destroys the profile of the red wing. To investigate this possibility, Hα is plotted on top of Hβ in Figure 12, as the profile of Hβ is not disturbed by anything and the profile should be similar to that of Hα. Since both Hα and Hβ have similar profile shapes, we can conclude that the Hα profile is indeed asymmetric up until 90 days.

The asymmetry can be explained by dust obscuring the radiation coming from the back of the ejecta, as the radiation coming towards us from the ejecta moving away from us is subjected more to the dust along its path [41], or it could be a
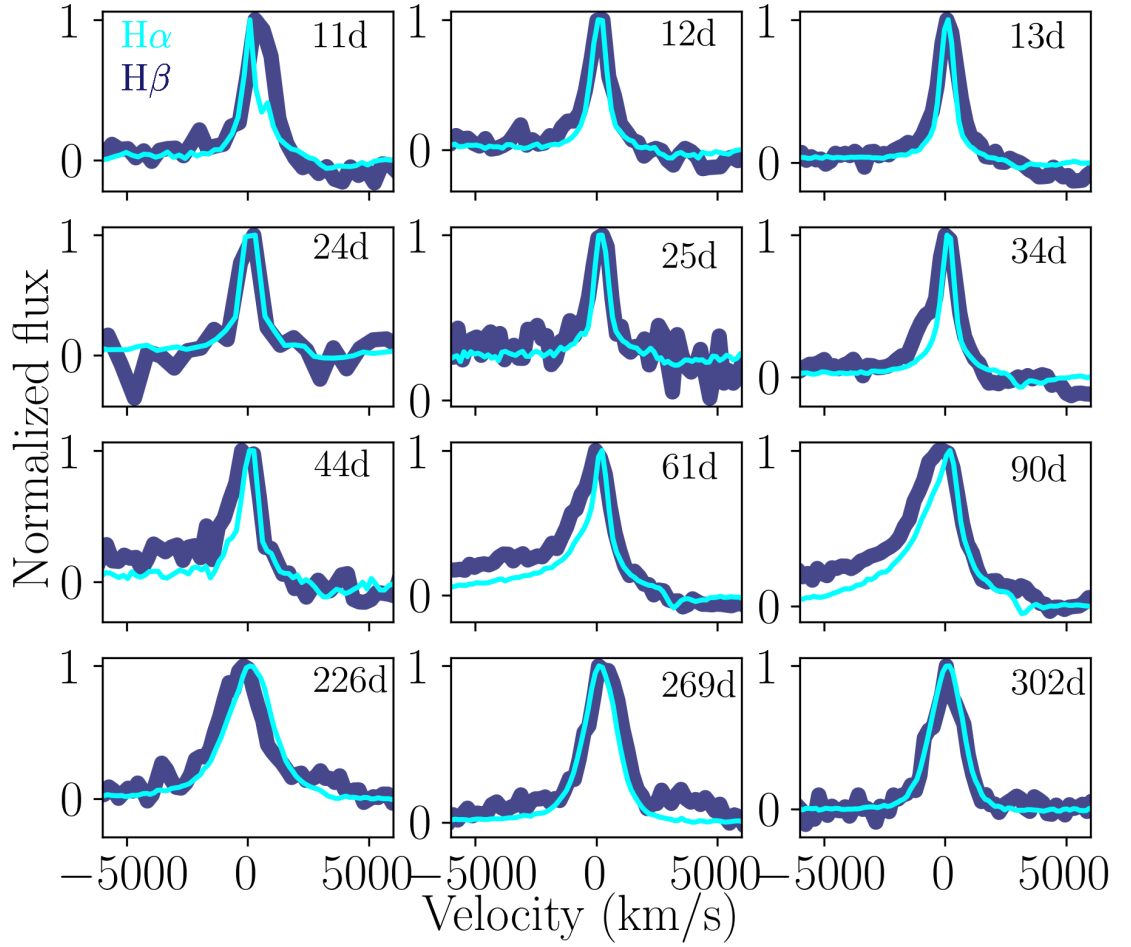
Figure 12. The Hα profile (cyan) plotted on top of the Hβ profile (blue). The epochs are listed as days in the right top corner of each panel. The Hα and Hβ have both been normalized and the x-axis is converted to velocity space to be able to plot them on top of each other.

product of the radiation that comes from the receding ejecta being occulted by an opaque photosphere. [42] As the Hα/Hβ stays relatively the same in the earlier epochs (see Figure 11), and there is no noticeable excess in NIR at 100 days from the explosion, we can conclude that the observations at early epochs are not affected by dust. The NIR excess will be discussed more in Section 4.2.

At late times, the Ca II NIR-triplet and the Fe features weaken, and only the Hα and Hβ lines are prominent. The Hα line gets narrower again, although it does not get as narrow as it was in the beginning. The profiles are well-fitted with a

Gaussian. The blackbody radius (see Figure 5, panel 2) seems to expand quite slowly until ∼225 days, whereafter it increases quickly. The Hα luminosity is highest at the epoch 226 days from the explosion. However, the reliability of this is uncertain as there were difficulties in the reduction and calibration of the spectra, as discussed in Section 2.3. In the last two epochs, the luminosity declines, which could be a sign that the SN ejecta has overtaken the majority of the CSM and that could possibly also hide the narrow component. It is also expected that the electron scattering optical depth becomes smaller as the SN shock propagates through the scattering circumstellar gas, making the mass motion the dominating factor in the spectra [40]. However, the Hα/Hβ flux ratio increases. This could be a sign of dust, as extinction is one of the ways to explain a different value for Balmer decrement assumed in case B recombination. Dust could also explain why SN 2017dio becomes redder at late times and the excess in NIR-bands. Dust, however, would make the Hα line asymmetric, and no clear sign of asymmetry is seen in the spectra at late times.

The velocities for the six first epochs of spectra is similar to each other as the Hα profile does not change significantly between these epochs. However, the velocities measured with both IRAF and Python show some variety. As seen from Figure 2, the Hα of the epoch 11d has a small peak disturbing the red side of the profile. When the Lorentzian was fit to this spectrum, IRAF tried to accommodate the peak and thus gave a larger velocity than should be expected. The Python code, on the other hand, seems to fit the Lorentzian higher than the actual peak, leading to the value of the FWHM being lower than it should be, which leads to the velocity also being lower, thus giving more of a lower limit for the velocity. A similar kind of behavior with fitting higher than the peak can also be seen in other epochs measured with Python, making the velocities measured from those lower limits as well. A good estimation of the velocities for the six epochs is approximately 400 km/s.

After 44 days up until 90 days, the Hα profile develops an asymmetric broad

Table VII. Table of the $H\alpha$ and $H\beta$ ratios. *The phase is given in days from the explosion.

Date (UT)	MJD	Phase* (d)	$\frac{H\alpha}{H\beta}$
2017-04-30	57873	11	2.28 ± 0.2
2017-05-01	57874	12	3.54 ± 0.35
2017-05-02	57875	13	2.77 ± 0.52
2017-05-13	57886	24	3.93 ± 2.34
2017-05-14	57887	25	4.05 ± 1.11
2017-05-23	57896	34	3.59 ± 0.26
2017-06-02	57906	44	3.53 ± 0.24
2017-06-19	57923	61	3.16 ± 0.32
2017-07-18	57952	90	3.80 ± 0.35
2017-12-01	58088	226	5.17 ± 1.68
2018-01-13	58131	269	8.54 ± 0.7
2018-02-15	58164	302	8.50 ± 0.48

component in the blue, which was discussed earlier in this section. These epochs are best fitted with two Lorentzian, one for the narrow component and the other for the intermediate component. The narrow component of the Hα emission line corresponds to the velocity of the wind (v_{wind}) and the intermediate component corresponds to the shock velocity (v_{shock}). For epochs 44d, 61d, and 90d, two Lorentzian were fitted with both IRAF and Python. The narrow component seems to be quite similar measured with IRAF and Python, and the broad components are in the error limits. The narrow component (wind velocity) seems to fluctuate, which might be because of the method used to do the measurements. On average, the wind velocity is approximately 500 km/s.

There is roughly a 140-day gap in observations between the ninth and tenth spectra, where the object went behind the Sun. During this time, it is impossible to know how the spectra evolve and how the velocity evolves. In the last three epochs, the Hα profile has started to narrow down again and become narrower through time. It is not as narrow as in the beginning. The last three epochs do not seem to show a narrow component anymore but are easily fit with one Lorentzian.

4.2   Light curve

The Light curves of SN 2017dio in *uBgcVroizJHK*-bands are plotted in Figure 13.

The *u*-band declines at the beginning of the light curve, but around 25 days starts to rise again. This happens to be around the same time that the spectra become dominated by interaction. The rest of the bands seem to be rising after the explosion, but looking closely at *g*- and *r*-band, a small "plateau" can be seen in the light curve, right before they start to rise more sharply. This sharp rise also starts at roughly the same time the *u*-band starts to rise and the interaction dominates the spectra. Similar rises cannot be seen in the other bands, as some of them lack the data (*BcVoJHK*), or the plateau is not clear enough to be certain it exists (*iz*).
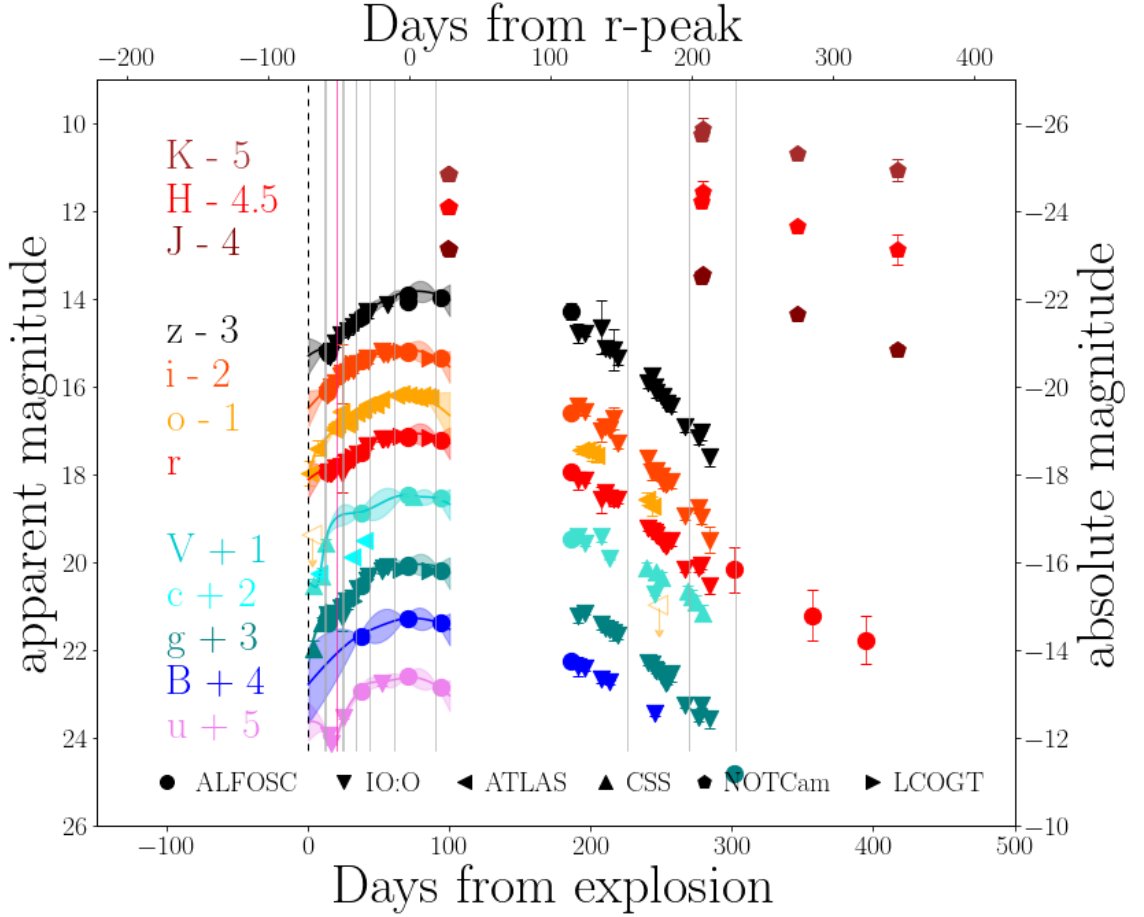
Figure 13. Light curve of SN 2017dio in *uBgcVroiz-* and *JHK*-bands. The left y-axis shows the apparent magnitude and the right y-axis absolute magnitude. Both are corrected for reddening. On x-axis we have days from the explosion. The photometric measurements acquired with the NOT using ALFOSC and NOTCam are marked with circles and pentagons, respectively. Data from the LT is marked with a downward triangle, CSS with an upward triangle, and ATLAS with a triangle pointing to the left, and LCOGT with triangles pointing to the right. A few non-detections (3σ) from ATLAS are marked with an orange, empty marker and an arrow downwards. The solid gray lines are the epochs for spectra and the dashed line is the day of the explosion.

Rise times for SN 2017dio are achieved by using Gaussian process and the results for peak absolute magnitude (reddening corrected) and rise time to peak can be seen in Table VIII. Rise time was not calculated for *cJHK*-bands because of the lack of data points. The rise to peak values varies from band to band, being quickest in *o*-band and slowest in *z*-band. Overall, the rise times for *u*- and *B*-band are slower than most of the other bands, making the rise times quite extraordinary. Normally,

SNe have quicker rise times in bluer bands, but for SN 2017dio this does not seem to be the case. This is easily explained by interaction. As mentioned earlier, u-band starts declining and rises again. One theory is, that the first "bump" is the decline of the SN itself and the peak is simply a result of the interaction. Similarly, the plateau in g- and r-band could be considered as the peak of the SN itself, and the rise in the light curve a consequence of the interaction. If the first "bump" seen in u-band and the plateau in g- and r-band are considered the SN peak, it fits the expectations that bluer bands evolve quicker. The fact that the temperature seems to increase as well, as can be seen from Figure 5, is consistent with interaction taking place. Assuming that the "plateau" is the peak of the SN itself, yields a peak absolute magnitude in the r-band of $\sim$-18 mag for the SN component. This SN peak magnitude as well as the rise time fits well with those of other SNe of type Ic-BL [43].

The LC has a gap when the object went behind the Sun. In NIR, the peak is either after or at the time the object is behind the Sun. Either way, the excess in NIR could be a sign of interaction. To further study the possibility of excess in NIR, SED-plots were constructed for epochs 100 and 279 days from the explosion. The SEDs are plotted in Figure 14. When I constructed the SEDs, I used the $BgVrizJHK$-bands and converted all of them into the Vega system. The $BVgriz$-bands for these dates were achieved by fitting a 4th-order polynomial to the photometric data. As seen from Figure 14 it is clear that there is some excess in NIR at later times. This excess could be related to the MIR detections mentioned in Thévenot *et al.* (2021). I fitted a blackbody on the NIR excess and gained a temperature of 1400 K. This temperature is an upper limit for the excess, as it is uncertain how the SED evolves in longer wavelengths.

The decline rates were calculated for $griz$-bands, as they are the only bands that were corrected for galaxy contamination. The decline rates were determined
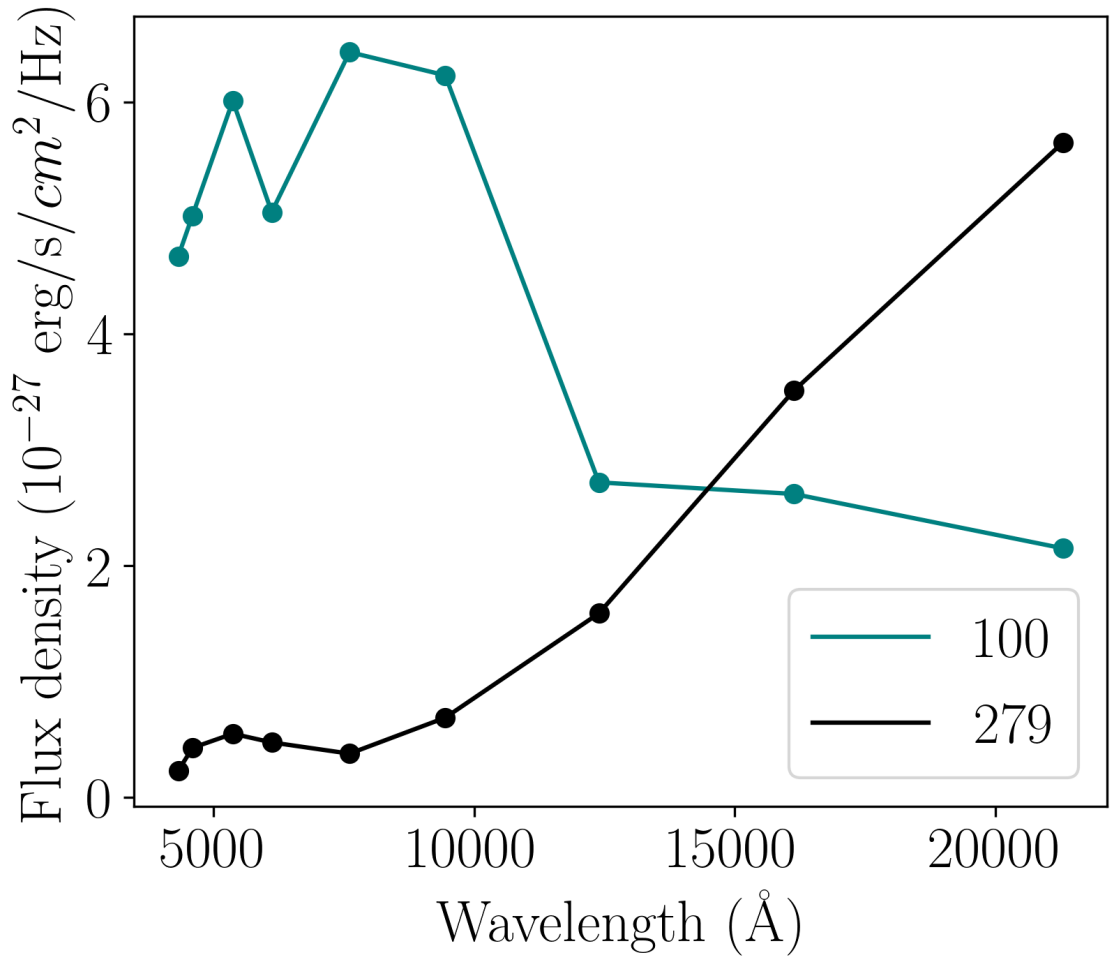
Figure 14. Spectral energy distribution (SED) constructed of *BgVrizJHK*-bands for epochs 100 and 279 days from the explosion. The x-axis is in wavelengths and the y-axis is in flux density.

by fitting a line to the data in the time range of 250 to 300 days. The decline rates can be seen in Table VIII. The decline rate for all the bands is approximately 0.038 mag/day, which makes SN 2017dio a quickly declining SN. The expected decay from ^{56}Co is 0.0098 mag/day, which is less than the decline rate of SN 2017dio. However, the bolometric light curve has a decline rate of 0.01 mag/day at late times, which follows the ^{56}Co radioactive decay. The bolometric light curve can be seen in Figure 4.

The radiated energy emitted by SN 2017dio is calculated by integrating over the bolometric light curve and is in the order $1.5 \cdot 10^{50}$ erg. The nickel mass is also

Table VIII. Peak absolute magnitudes (Peak abs. Mag), rise times, and decline rates for SN 2017dio in different bands.

Band	Peak abs. Mag (mag)	Rise time (d)	Decline rate (mag/day)
u	-18.65 ± 0.10	74 ± 2	
B	-18.72 ± 0.18	73 ± 2	
g	-18.96 ± 0.02	69 ± 1	0.038
V	-18.52 ± 0.01	67 ± 2	
r	-18.94 ± 0.13	72 ± 2	0.034
o	-18.83 ± 0.02	66 ± 1	
i	-18.86 ± 0.03	70 ± 1	0.039
z	-19.18 ± 0.21	78 ± 4	0.040

calculated using Arnett's rule [44]

$$M_{\mathrm{Ni}} = \frac{L_{\mathrm{peak}}}{(\epsilon_{\mathrm{Ni}} - \epsilon_{\mathrm{Co}})e^{-t_{\mathrm{p}}/t_{\mathrm{Ni}}} + \epsilon_{\mathrm{Co}}e^{-t_{\mathrm{p}}/t_{\mathrm{Co}}}} \qquad (15)$$

where M_{Ni} is the nickel mass, L_{peak} is the peak bolometric luminosity, $\epsilon_{\mathrm{Ni}} = 3.9 \cdot 10^{10}$ erg/g/s and $\epsilon_{\mathrm{Co}} = 6.8 \cdot 10^{9}$ erg/g/s are the specific heating rates of Ni and Co decay, $t_{\mathrm{Ni}} = 8.8$ days and $t_{\mathrm{Co}} = 111.3$ days are the decays scales of Ni and Co and t_{p} is the rise time [44]. For the nickel mass estimation, we assume that the $L_{\mathrm{peak}} = 1.14 \cdot 10^{43}$ and $t_{\mathrm{p}} = 70$ days (peak data point in Figure 4). With these, we get $M_{\mathrm{Ni}} \approx 1.6 M_{\odot}$. The nickel mass achieved is unrealistically high and the reason for this is that the bolometric luminosity and peak time were used, even though the light curve is mostly powered by interaction and not radioactive decay. If we, however, choose the bolometric luminosity at roughly 25 days after the explosion (when interaction seems to start dominating the light curves), and use $t_{\mathrm{p}} = 20$, we get $M_{\mathrm{Ni}} \approx 0.3 M_{\odot}$, which is consistent with nickel masses of other type Ic-BL SN [45].

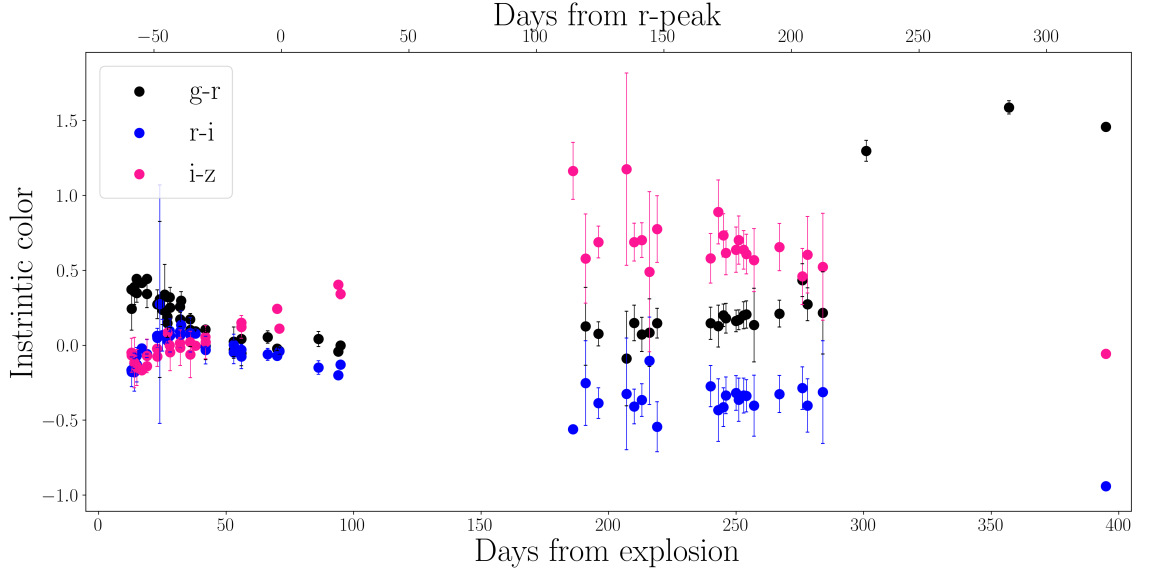The color curves of SN 2017dio are plotted as g-r, r-i, and i-z in Figure 15. In

Figure 15. Intrinsic colors of SN 2017dio. The x-axis is in days from explosion (lower) and in days from r-peak (upper).

g-r, the SN becomes quickly red after the explosion but starts to get bluer after approximately 15 days. This is around the same time both g- and r-band have their plateau in the light curve. When the interaction starts to show in the light curve, the color curve also gets bluer. Meanwhile, both *r-i* and *i-z* have a slower-evolving color curve, becoming redder approximately to the peak.

After the peak, *g-r* and *r-i* are evolving similarly, getting bluer and stabilizing after the data gap. At the same time, the spectra start to show stronger lines in Ca, making the *i-z* evolve redder.

4.3 Blackbody parameters

Normally, type Ic-BL SNe show a progressive decline in temperature from the explosion date to ~25 days, where it flattens out at ~6000 K [43]. The blackbody temperature of the SN 2017dio seems to rise with the light curve and hits its peak at approximately 8500 K roughly the same time as the light curves reach their peaks (see Figure 5). It is arguable if SN 2017dio follows the progressive decline consistent with non-interacting SNe Ic-BL at the first 25 days. The temperature achieved with

Superbol does not include data for the first 15 days, and the blackbodies fitted on top of the spectra (see Figure 6) give only data for ∼10 days after the explosion. However, what we can see from here is that the temperature is fluctuating and there might be a small decline until ∼25 days when the interaction starts and the temperature rises again. The spectra are also affected by suppression of the blue flux due to line blanketing, so the fits are more of an estimation.

The radius of the blackbody grows slightly in the first 100 days, but after 200 days the radius starts to grow faster, while the temperature in turn decreases.

4.4   Comparison

SN 2017dio is now compared with four other SNe. The comparison SNe were chosen by finding close spectral matches for 2017dio at three epochs. The matches were found by using GELATO [46] and SNID [47]. The first spectra used to find comparison SNe is 2017-04-30, which was taken 11 days after the explosion of SN 2017dio. This spectrum still shows the underlying SN component and one of the closest matches for this epoch is the type Ic-BL SN 2006aj [48]. The second spectrum used is 2017-05-14, where the interaction dominates and a close match for this epoch is the type IIn (Ia-CSM) SN 2005gj. The last spectrum is 2017-07-18, which shows the bump in bluer parts of the spectrum and Ca II NIR-triplet. The closest match for this epoch is the type IIn SN 2009ip. So SN 2005gj, SN 2006aj, and SN 2009ip are the closest matches for the three different epochs of SN 2017dio. SN 2017ens was chosen as well, as it is a similar object to SN 2017dio. SN 2017ens also starts as a type Ic SN that then evolves to a type IIn. The comparison SNe and their information can be seen in Table IX.

The light curves of the comparison SNe and SN 2017dio are plotted in Figure 16. The light curve of SN 2017dio does not resemble any of the comparison light curves. The rise to the peak is slowest for SN 2017dio, although it shares a similar

Table IX. Table containing the name, type, redshift z, explosion epoch in MJD, r-peak, and decline rate of the comparison objects. *The explosion epoch for 2006aj is considered to be the date of the GRB burst and **the explosion epoch for 2009ip is considered to second discovery in 2012.

SN	type	z	exp. epoch (MJD)	r-peak (d)	Decline rate (mag/day)	ref. spectra phot
2005gj	IIn	0.0616	53637.43	30	0.014	[49][50]
2006aj	Ic-BL	0.033	53784*	11	0.079	[51][52]
2009ip	IIn	0.005944	56132.5**	75	0.051	[53][54]
2017ens	SLSN	0.1086	57907.8	10	0.036	[55]

r-peak time with SN 2009ip. The peak magnitude is similar to SN 2006aj, but the evolution of SN 2006aj is much faster than that of SN 2017dio. As SN 2006aj is also classified as type Ic-BL SN, the evolution of its light curve could give some kind of idea of the evolution of the underlying SN light curve of SN 2017dio, pre-interaction. Assuming a similar evolution for the underlying SN light curve as SN 2006aj, most of SN 2017dio's light curve must be powered by something else, most likely the interaction.

The approximate decline rates in the r-band for the comparison objects were calculated similarly to SN 2017dio's and can be found in Table IX. The decline rate for SN 2017ens was calculated from the data right after the peak. The decline rate of SN 2005gj is closest to SN 2017dio, being only approximately 0.004 mag/day slower. The other comparison objects decline quicker, and as expected.

Figure 17 plots the g-r values for SN 2017dio and the comparison objects. As expected, SN 2017dio has a similar rise as SN 2006aj and SN 2009ip in the beginning and becomes redder. When the interaction starts to dominate the spectra, SN 2017dio starts to behave more like SN 2009ip and becomes bluer. It no longer behaves like SN 2006aj. SN 2017dio continues to become bluer for a longer period
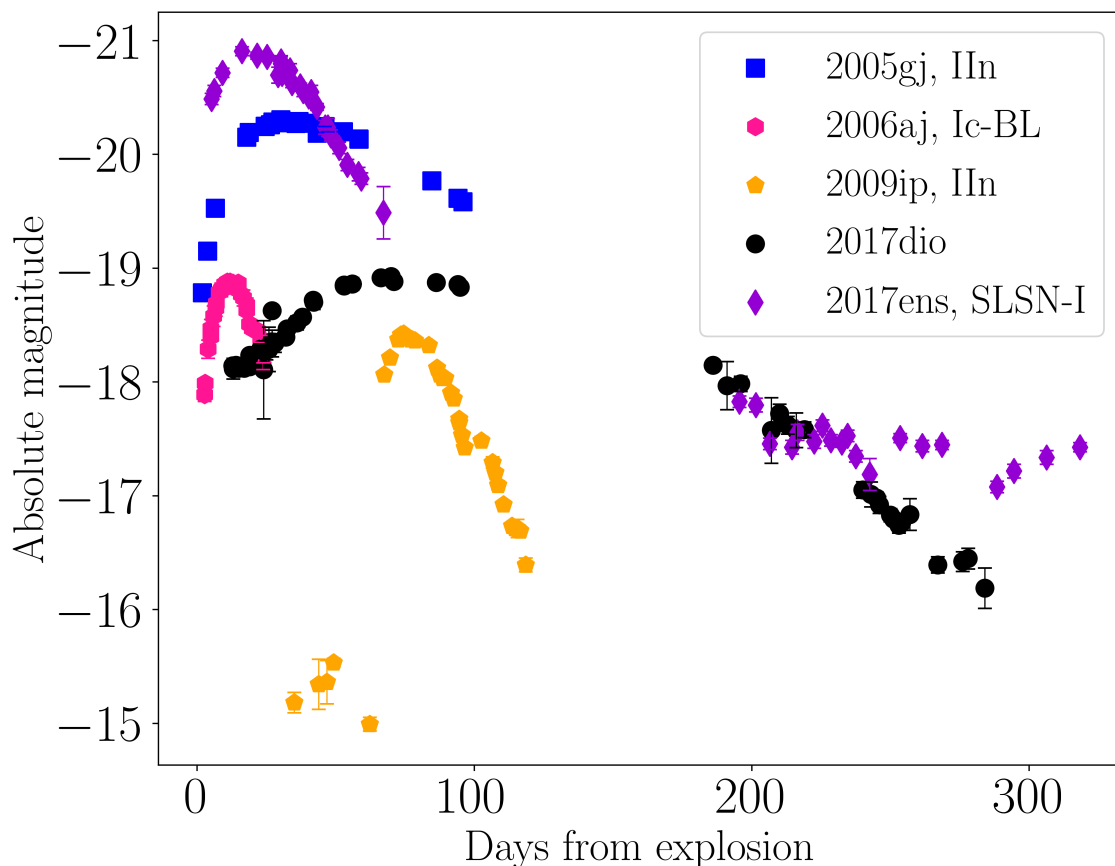
Figure 16. Comparing the light curve of SN 2017dio in r-band with the light curves of SN 2005gj, SN 2006aj, SN 2009ip and SN 2017ens, also in r-band. The light curves of SN 2006aj and SN 2009ip are in the R-band, SN 2005aj and SN 2017ens in the r-band. In the Figure, the data of SN 2005gj is plotted with blue squares, SN 2006aj with pink hexagons, SN 2009ip with yellow pentagons and SN 2017ens with violet diamonds. The y-axis is in absolute magnitudes and the x-axis is from days from explosion.

of time than SN 2009ip. Except for getting redder in the beginning, SN 2017dio does not seem to share any similarities with SN 2005gj or SN 2017ens in the given time period.

As for the spectroscopic similarities, three epochs of SN 2017dio spectra are compared with the comparison SNe. The three different epochs were chosen so that they showed the evolution of SN 2017dio spectra and the comparison SNe spectra were chosen at similar epochs. The comparisons are plotted in Figure 18.
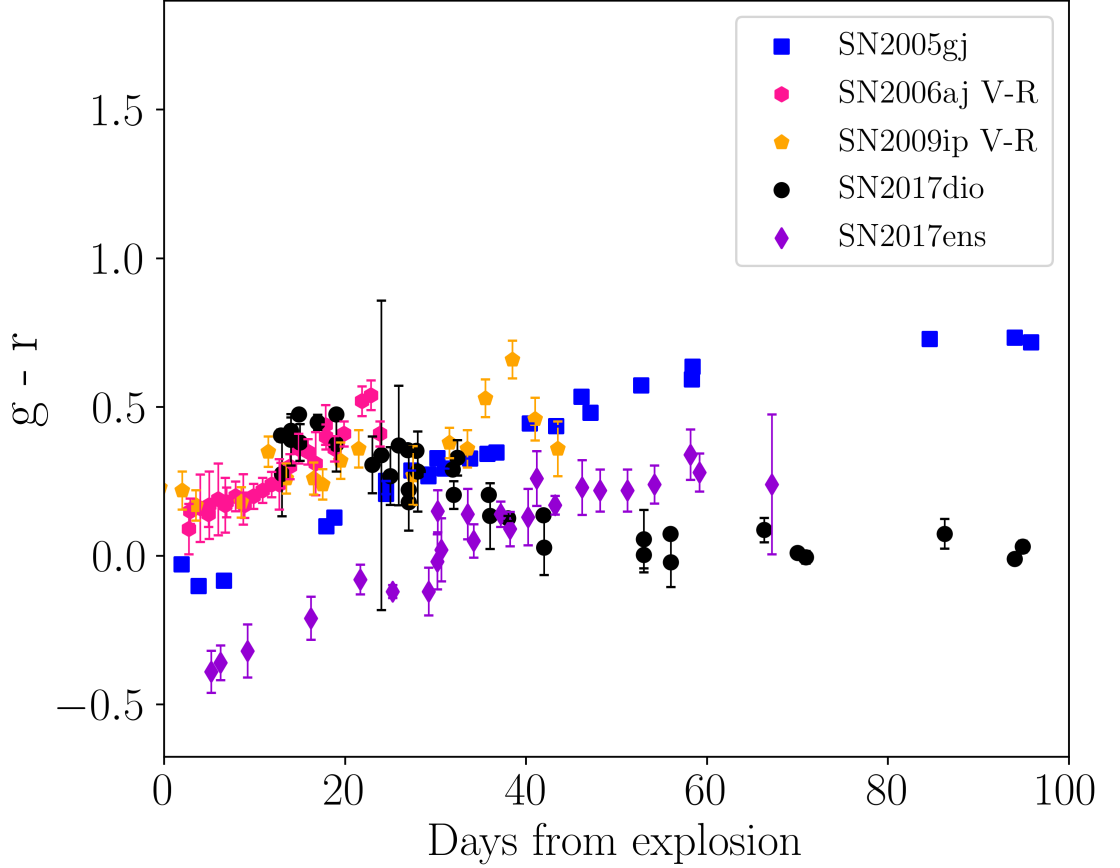
Figure 17. Color (g-r) curve comparison of SNe 2017dio, 2005gj, 2006aj, 2009ip and 207ens from explosion to 100 days.

The first epoch is from 11 days from the explosion, where the SN 2017dio spectrum shows the underlying SN Ic-BL spectra with superimposed narrow Balmer emission lines. This epoch was compared with SN 2005gj and SN 2006aj. At this time, the spectrum of SN 2017dio resembles the spectrum of SN 2006aj. Both spectra have similar broad absorption features that are known to be a feature of type Ic-BL SN. The broad absorption features of SN 2006aj seem to be more blue-shifted than those of SN 2017dio, meaning that the expansion velocities are more likely lower for SN 2017dio. To further analyse the Ic-BL classification, a "pure" SN component was made. The pure SN component was done by subtracting the interaction-dominated spectrum from the spectrum that still showed the SN-type features. Both spectra were normalized before the subtraction, and the remaining
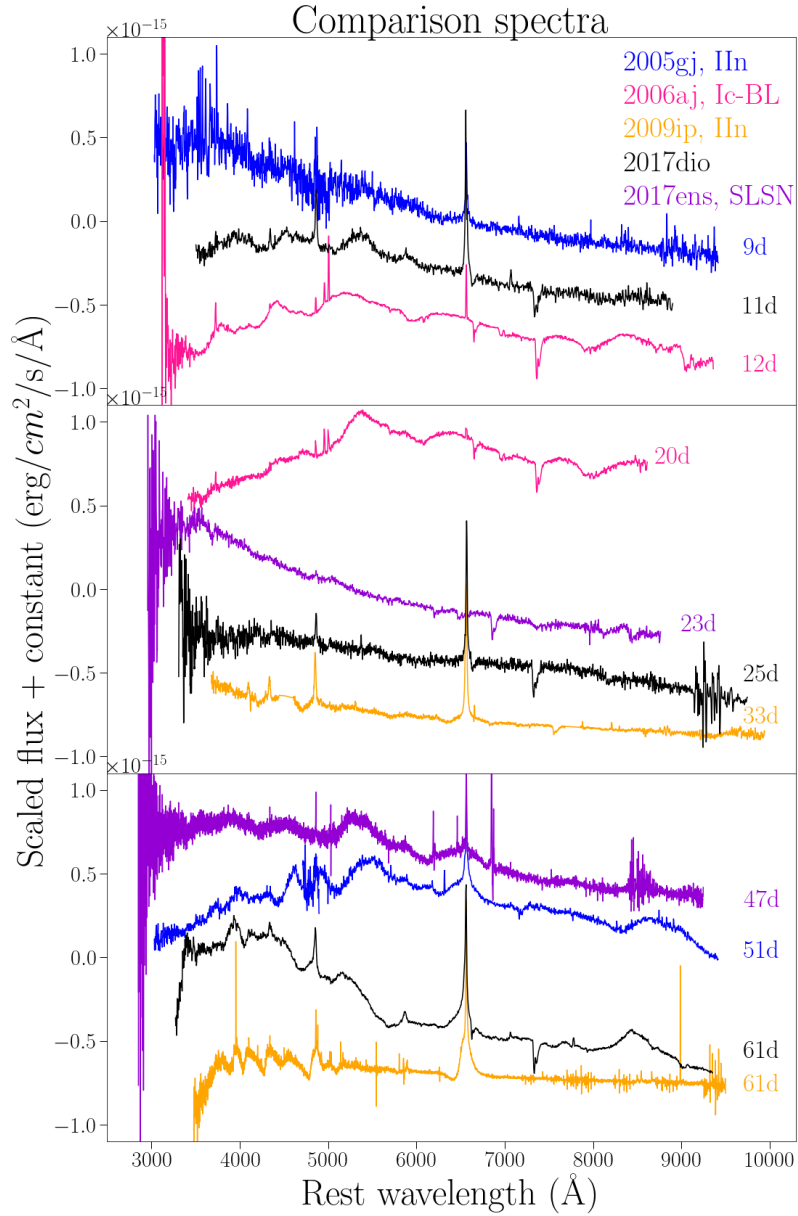
Figure 18. Comparison spectra. Three different epochs of supernova (SN) 2017dio spectra have been plotted in three different panels alongside the comparison spectra. SN 2005gj in blue, SN 2006aj in pink, SN 2009ip in yellow, SN 2017dio in black, and SN 2017ens in violet. In the first panel, the epoch is approximately 10 days from the explosion, where the 2017dio spectra still resemble that of a Ic-BL SN. In the second panel, the epoch is approximately 25 days from the explosion, which is when the spectra become dominated by the interaction and appear featureless, except for the narrow H emission lines. In the last panel, the epoch is approximately 60 days from the explosion and this is when the SN 2017dio spectra evolve a bump in the bluer parts and Ca II near infrared-triplet in the redder parts.

Hα and Hβ line excess was removed. The pure SN spectra are plotted in Figure 19. Using GELATO to classify the spectra gives a good match with a SN of type Ic-BL, although the confidence level is not high and the spectra cannot be compared.

The only resemblance to SN 2005gj at this epoch is the narrow Hα emission line that is a signature of interaction.

The second epoch is 25 days from the explosion, where the spectrum gets dominated by the interaction and no sign of the underlying SN type can be distinguished. This epoch is compared with SN 2006aj, which still shows broad absorption features and no longer resembles the spectrum of SN 2017dio. The spectrum is also compared with that of SN 2009ip and SN 2017ens, which both show a similar featureless spectrum. Both SN 2009ip and SN 2017dio have strong narrow Hα and Hβ emission lines, but for SN 2017ens, the lines are barely recognizable.

The last epoch is 61 days from the explosion and at this time the spectrum of SN 2017dio has developed more features and shows a bump in the bluer parts of the spectrum, narrow He emission lines, and the Ca II NIR-triplet emission. This epoch is compared with SN 2005gj, SN 2009ip, and SN 2017ens. Similar kinds of bumps that SN 2017dio has can be seen in the spectra of SN 2009ip and SN 2017ens, although the spectra for those do not have as good of a resolution as the spectrum of SN 2017dio has. While all of the spectra show the narrow H emission lines, only SN 2005gj has the Ca II NIR-triplet in the redder part of the spectrum.

In conclusion, SN 2017dio has a slower rise to the peak than any of the compared SNe. It shares early-time spectral similarities with SN 2006aj, but evolves to resemble those of type IIn at later times.

4.5   CSM and progenitor analysis

The spectra of SN 2017dio start off by looking like a type Ic-BL SN with narrow emission lines superposed on the spectra and evolve approximately 25 days after

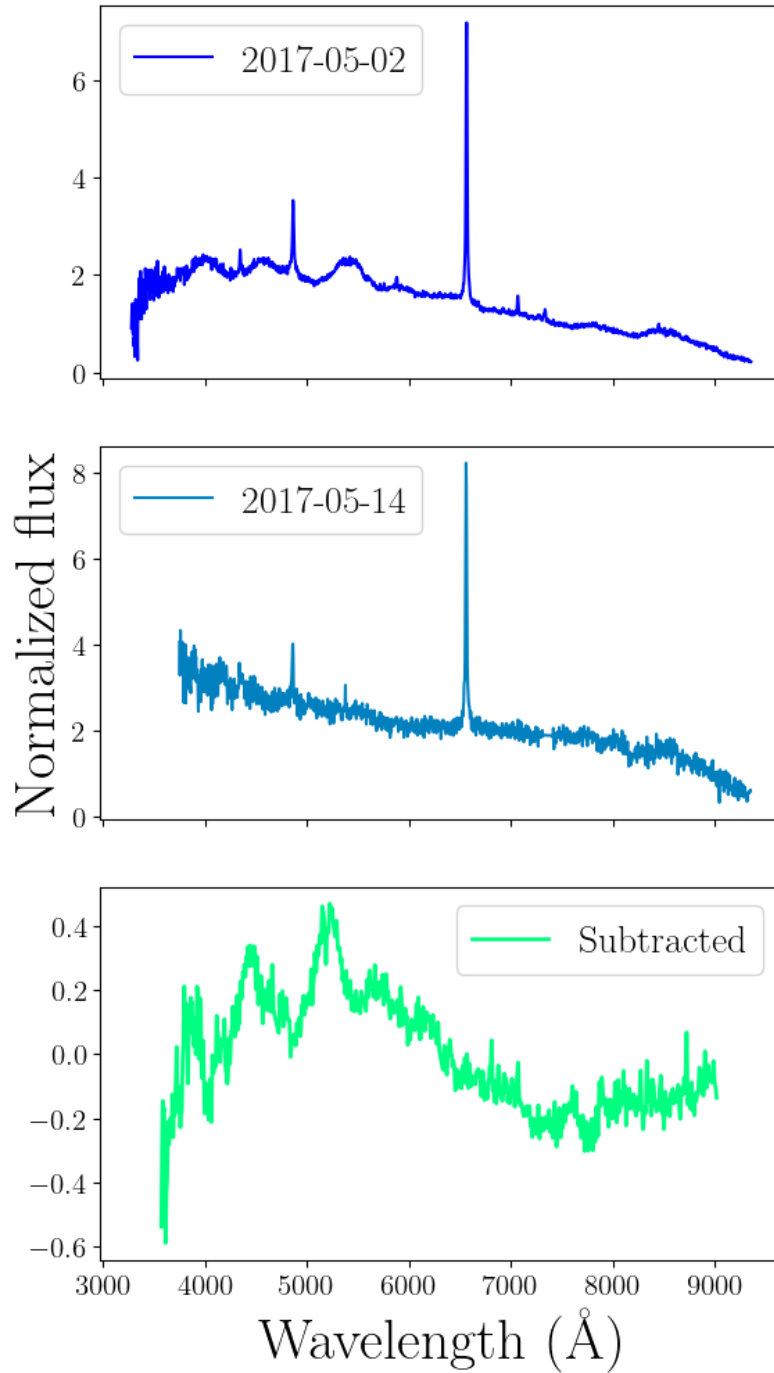Figure 19. The pure supernova (SN) component of SN 2017dio. The pure SN component was acquired by subtracting the interaction-dominated spectrum (panel 2) from the spectrum that still showed the underlying SN-type features (panel 1). Both spectra were normalized by the mean flux and the pure SN component was then smoothed and the remaining Hα and Hβ lines were removed. Panel 3 shows the subtracted, "pure" SN component.

the explosion to look like a type IIn. At the same time, the light curves in *ugr*-bands start to rise more sharply. Both the spectra and the delayed peak in the light curve indicate that the interaction was relatively weak in early epochs and that the CSM does not lie close to the SN. The broadening of the emission lines and the increase of Hα luminosity, indicate that the interaction gets stronger with time. When the forward shock hits the CSM, the interaction gets stronger and the emission lines get an intermediate component. This happens around 44 days after the SN explosion and if we further assume that the velocity of the shock corresponds to the intermediate component at that time ($v_{\text{shock}} \approx 9100$ km/s) and the wind velocity corresponds to the average value of the narrow component ($v_{\text{wind}} \approx 500$ km/s), then we can calculate how far the CSM is located. The shock velocity was chosen to be the one that was measured with IRAF, since the error for that one was smaller. Assuming homologous expansion, we can calculate that the shock has moved approximately 230 AU before it hits the CSM. If the wind speed is assumed constant, then the last of the CSM must have been ejected around two years before the SN explosion.

The densest part of the CSM lies where the Hα luminosity is strongest. As it is unclear how the interaction evolves when the object is behind the Sun, it is possible that the H emission lines in the last three spectra are from a different CSM or that the CSM varies greatly in density. For the CSM distance and mass loss calculations, we take the luminosity of Hα at around 90 days from the explosion, as the luminosity achieved from 220 days might be unreliable. Making the same assumptions as earlier ($v_{\text{wind}} = 500$ km/s and $v_{\text{shock}} = 9100$ km/s) we get that the densest part of the CSM lies at 475 AU from the explosion site and was ejected more than 4.5 years before the explosion.

The mass loss at these times can be estimated with

$$\dot{M} = 2 \frac{L_{\text{H}\alpha}}{\epsilon_{\text{H}\alpha}} \frac{v_{\text{wind}}}{v_{\text{shock}}^3} \tag{16}$$

where $L_{\text{H}\alpha}$ is the luminosity of Hα at the time and $\epsilon_{\text{H}\alpha}$ is the efficiency factor 0.01.[56] The mass loss to create the densest part of the CSM is approximately $\dot{M} = 0.04 M_{\odot}/$year. It is easy to say that if the CSM indeed originated from the progenitor itself, it must have experienced massive mass loss periods in the last decade before its explosion, maybe even before that.

Kuncarayakti *et al.* (2018) came to the conclusion that the geometry of the CSM is asymmetric and that the progenitor is a binary. These conclusions are compared with the results achieved in this thesis.

As already mentioned, the underlying SN type was visible for roughly 20 days before the interaction took over. This means that the CSM is not near the surface of the SN progenitor and is not produced from spherically symmetric mass loss. The Hα/Hβ flux ratio can be calculated for a given temperature and electron density, assuming case B recombination. In case B recombination, the flux ratio should have a value of ∼3 [57] (assuming temperature = 5000 K). The values of the Hα/Hβ are around the expected value in early times but do seem to fluctuate around it. If the Hα/Hβ ratio can be used to explain density in the CSM, then there might be fluctuations in the CSM density as suggested by Kuncarayakti *et al.* (2018). It is evident that the CSM geometry is not spherically symmetric and what kind of form it has is hard to tell. It could be clumpy like predicted for SN 2005gj [50], or it could be toroidal like SN 2009ip [54].

The CSM is H-rich, which is clear as the spectra show the narrow H emission lines. It also has some helium but would be mostly considered He-poor. For SE SNe, it is common to lose first the hydrogen envelope (as it is the outermost shell of a star) and the helium envelope after that. If the progenitor of SN 2017dio is a single star, the CSM should have more helium in it. The fact that only little helium is visible in the spectra, suggests that the progenitor is a binary. This conclusion is consistent with Kuncarayakti *et al.* (2018). In the binary theory, the more massive

star (progenitor of SN 2017dio in this case) evolves and starts to transfer mass to the other star through a Roche-lobe and is left as C+O star (no H or He left) [58]. The other star then gets more massive, which accelerates its evolution and it will in turn start to transfer mass to the progenitor of SN 2017dio. This would make the surroundings H-rich and when the progenitor eventually explodes, it would produce a type Ic SN (no H or He left in the ejecta) and as the CSM would be H-rich, we get H emission lines from the interaction.

5 Conclusion

In this thesis, the photometric and spectroscopic analysis of the interacting SN 2017dio was done. SN 2017dio is classified as a type Ic-BL SN that evolves into a type IIn SN.

The photometric data were used to construct light curves that were again used to determine rise times and peak magnitudes and compared to other SNe. The light curves of SN 2017dio show two different components, the first component originating from the SN itself and the other from the interaction. The SN component compares well with other types of Ic-BL SNe, while the light curve powered by the interaction has a long rise time and does not compare well with the comparison SNe used in this thesis. The radiative energy emitted by SN 2017dio is $1.5 \cdot 10^{50}$ erg, which is high compared with non-interacting SNe. The photometric data were also used to determine the explosion epoch, which is 2017-04-19 (MJD=57861.95).

The spectroscopic data was used to confirm the classification of SN 2017dio and to study the evolution of the interaction. The spectra of SN 2017dio start off by looking like that of SN 2006aj, which is a Ic-BL SNe. At a later epoch, SN 2017dio evolved to look like SN 2009ip and SN 2017ens, which are both interacting SNe, verifying that SN 2017dio indeed transitions from a type Ic-BL to a type IIn.

The Hα line was studied more closely and velocities were measured for different

epochs. The wind velocity stays relatively the same, but around 44 days from the explosion, shock velocity can be determined. These were used to estimate mass loss, distance to the CSM, and when the mass loss happened. The achieved mass loss rate is $0.04_\odot$/year. Hα luminosity and the Hα/Hβ ratio were used to study the properties of the CSM. The density of the CSM is asymmetric in nature. It is also hydrogen-rich and most likely from a binary progenitor.

In conclusion, SN 2017dio is an interesting object that can shed light on what happened during the last moments of its progenitor's life. Analysing SNe like this gives new information about stellar evolution that can be crucial when developing better stellar evolution models and understanding how massive stars evolve. As for future work, it would be interesting to try and differentiate the CSM component and the supernova component in the light curve and try to analyse the nickel mass and ejecta mass based on the SN component. I will also look more into the MIR study mentioning SN 2017dio and compare it more with the findings done in this work. I also plan on getting the work submitted in a refereed journal article.

Acknowledgements

References

[1] A. V. Filippenko. "Optical Spectra of Supernovae". In: *Annual Review of Astronomy and Astrophysics* 35 (1997), pp. 309–355. DOI: 10.1146/annurev.astro.35.1.309.

[2] S. P. Owocki, G. E. Romero, R. H. D. Townsend, and A. T. Araudo. "Gamma-Ray Variability from Wind Clumping in High-Mass X-Ray Binaries with Jets". In: *The Astrophysical Journal* 696 (2009), pp. 690–693. DOI: 10.1088/0004-637X/696/1/690.

[3] S. E. Woosley, A. Heger, and T. A. Weaver. "The evolution and explosion of massive stars". In: *Reviews of Modern Physics* 74 (2002), pp. 1015–1071. DOI: 10.1103/RevModPhys.74.1015.

[4] N. Smith. "Mass Loss: Its Effect on the Evolution and Fate of High-Mass Stars". In: *Annual Review of Astronomy and Astrophysics* 52 (2014), pp. 487–528. DOI: 10.1146/annurev-astro-081913-040025.

[5] E. Pian and P. A. Mazzali. "Hydrogen-Poor Core-Collapse Supernovae". In: *Handbook of Supernovae*. Ed. by Athem W. Alsabti and Paul Murdin. 2017, p. 277. DOI: 10.1007/978-3-319-21846-5_40.

[6] N. Smith. "Interacting Supernovae: Types IIn and Ibn". In: *Handbook of Supernovae*. Springer International Publishing, 2017, pp. 403–429. DOI: 10.1007/978-3-319-21846-5_38.

[7] M. C. Bersten and P. A. Mazzali. "Light Curves of Type I Supernovae". In: *Handbook of Supernovae*. Ed. by A. W. Alsabti and P. Murdin. Cham: Springer International Publishing, 2017, pp. 723–735. ISBN: 978-3-319-21846-5. DOI: 10.1007/978-3-319-21846-5_25.

[8] H. Junde, H. Su, and Y. Dong. "Nuclear Data Sheets for A = 56". In: *Nuclear Data Sheets* 112.6 (2011), pp. 1513–1645. DOI: 10.1016/j.nds.2011.04.004.

[9] O. D. Fox et al. "A SPITZER SURVEY FOR DUST IN TYPE IIn SUPERNOVAE". In: *The Astrophysical Journal* 741 (2011), p. 7. DOI: 10.1088/0004-637X/741/1/7.

[10] H. Kuncarayakti et al. "SN 2017dio: A Type-Ic Supernova Exploding in a Hydrogen-rich Circumstellar Medium". In: *The Astrophysical Journal Letters* 854 (2018), p. L14. DOI: 10.3847/2041-8213/aaaa1a.

[11] M. Thévenot, J. M. Gantier, M. Kabatnik, J. Schümann, and L. Gramaize. "Mid-infrared Detections of Type I Supernovae and Unclassified Possible Supernovae with NEOWISE". In: *Research Notes of the American Astronomical Society* 5 (2021), p. 58. DOI: 10.3847/2515-5172/abf120.

[12] J. L. Tonry et al. "ATLAS: A High-cadence All-sky Survey System". In: *Publications of the Astronomical Society of the Pacific* 130 (2018). DOI: 10.1088/1538-3873/aabadf.

[13] *SN 2017dio*. https://www.wis-tns.org/object/2017dio.

[14] K. W. Smith et al. "Design and Operation of the ATLAS Transient Science Server". In: *Publications of the Astronomical Society of the Pacific* 132 (2020). DOI: 10.1088/1538-3873/ab936e.

[15] L. Shingles et al. "Release of the ATLAS Forced Photometry server for public use". In: *Transient Name Server AstroNote* 7 (2021), pp. 1–7.

[16] B. Abolfathi et al. "The Fourteenth Data Release of the Sloan Digital Sky Survey: First Spectroscopic Data from the Extended Baryon Oscillation Spectroscopic Survey and from the Second Phase of the Apache Point Observatory Galactic Evolution Experiment". In: *The Astrophysical Journal Supplement Series* 235 (2018), p. 42. DOI: 10.3847/1538-4365/aa9e8a.

[17] R. M. Barnsley et al. "IO:I, a near-infrared camera for the Liverpool Telescope". In: *Journal of Astronomical Telescopes, Instruments, and Systems* 2 (2016), p. 015002. DOI: 10.1117/1.JATIS.2.1.015002.

[18] A. J. Drake et al. "First Results from the Catalina Real-Time Transient Survey". In: *The Astrophysical Journal* 696 (2009), pp. 870–884. DOI: 10.1088/0004-637X/696/1/870.

[19] T. M. Brown et al. "Las Cumbres Observatory Global Telescope Network". In: *Publications of the Astronomical Society of the Pacific* 125 (2013), p. 1031. DOI: 10.1086/673168.

[20] S. J. Brennan and M. Fraser. "The Automated Photometry of Transients pipeline (AUTOPHOT)". In: *Astronomy Astrophysics* 667 (2022). DOI: 10.1051/0004-6361/202243067.

[21] A. A. Henden et al. "APASS Data Release 10". In: *American Astronomical Society Meeting Abstracts #232*. Vol. 232. American Astronomical Society Meeting Abstracts. 2018, p. 223.06.

[22] M. F. Skrutskie et al. "The Two Micron All Sky Survey (2MASS)". In: *The Astronomical Journal* 131 (2006), pp. 1163–1183. DOI: 10.1086/498708.

[23] P. W. Draper, N. Gray, D. S. Berry, and M. Taylor. *GAIA: Graphical Astronomy and Image Analysis Tool.* Astrophysics Source Code Library, record ascl:1403.024. 2014.

[24] *ALFOSC grisms.* https://www.not.iac.es/instruments/alfosc/grisms/.

[25] *EFOSC2 grisms.* https://www.eso.org/sci/facilities/lasilla/instruments/efosc/inst/Efosc2Grisms.html.

[26] *SPRAT grism.* https://telescope.livjm.ac.uk/TelInst/Inst/SPRAT/.

[27] D. Tody. "The IRAF Data Reduction and Analysis System". In: *Instrumentation in astronomy VI.* Ed. by David L. Crawford. Vol. 627. Society of Photo-Optical Instrumentation Engineers (SPIE) Conference Series. 1986, p. 733. DOI: 10.1117/12.968154.

[28] E. F. Schlafly and D. P. Finkbeiner. "Measuring Reddening with Sloan Digital Sky Survey Stellar Spectra and Recalibrating SFD". In: *The Astrophysical Journal* 737.2 (2011), p. 103. DOI: 10.1088/0004-637X/737/2/103.

[29] G. V. Schultz and W. Wiemer. "Interstellar reddening and IR-excesses of O and B stars." In: *Astronomy and Astrophysics* 43 (1975), pp. 133–139.

[30] R. Cartier, C. Gutierrez, and O. Yaron. "ePESSTO Transient Classification Report for 2017-04-30". In: *Transient Name Server Classification Report* 2017-500 (2017), p. 1.

[31] J. A. Cardelli, G. C. Clayton, and J. S. Mathis. "The Relationship between Infrared, Optical, and Ultraviolet Extinction". In: *The Astrophysical Journal* 345 (1989), p. 245. DOI: 10.1086/167900.

[32] C. Rodrigo and E. Solano. "The SVO Filter Profile Service". In: *XIV.0 Scientific Meeting (virtual) of the Spanish Astronomical Society*. 2020, p. 182.

[33] D. Poznanski, J. X. Prochaska, and J. S. Bloom. "An empirical relation between sodium absorption and dust extinction". In: *Monthly Notices of the Royal Astronomical Society* 426 (Oct. 2012), pp. 1465–1474. DOI: 10.1111/j.1365-2966.2012.21796.x.

[34] A. Almeida et al. "The Eighteenth Data Release of the Sloan Digital Sky Surveys: Targeting and First Spectra from SDSS-V". In: *The Astrophysical Journal Supplement Series* 267 (2023), p. 44. DOI: 10.3847/1538-4365/acda98.

[35] D. J. Schlegel, D. P. Finkbeiner, and M. Davis. "Maps of Dust Infrared Emission for Use in Estimation of Reddening and Cosmic Microwave Background Radiation Foregrounds". In: *The Astrophysical Journal* 500 (1998), pp. 525–553. DOI: 10.1086/305772.

[36] M. Nicholl. *SUPERBOL: Supernova Bolometric Light Curves*. https://github.com/mnicholl/superbol/blob/master/superbol.py.

[37] A. Lee H. F. Stevance. "What can Gaussian Processes really tell us about supernova lightcurves? Consequences for Type II(b) morphologies and genealogies". In: *Astroph-SR* (2022).

[38] C. E. Rasmussen and C. K. I. Williams. *Gaussian processes for machine learning.* Adaptive computation and machine learning. MIT Press, 2006, pp. I–XVIII, 1–248. ISBN: 026218253X.

[39] J. Deng et al. "Subaru Spectroscopy of the Interacting Type Ia Supernova SN 2002ic: Evidence of a Hydrogen-rich, Asymmetric Circumstellar Medium". In: *The Astrophysical Journal* 605 (2004), pp. L37–L40. DOI: 10.1086/420698.

[40] C. Huang and R. A. Chevalier. "Electron scattering wings on lines in interacting supernovae". In: *Monthly Notices of the Royal Astronomical Society* 475 (2018), pp. 1261–1273. DOI: 10.1093/mnras/stx3163.

[41] A. Bevan and M. J. Barlow. "Modelling supernova line profile asymmetries to determine ejecta dust masses: SN 1987A from days 714 to 3604". In: *Monthly Notices of the Royal Astronomical Society* 456 (2015), pp. 1269–1293. ISSN: 0035-8711. DOI: 10.1093/mnras/stv2651.

[42] F. Taddia et al. "Carnegie Supernova Project: Observations of Type IIn supernovae". In: *Astronomy & Astrophysics* 555 (2013), A10. DOI: 10.1051/0004-6361/201321180. URL: https://doi.org/10.1051%2F0004-6361%2F201321180.

[43] F. Taddia et al. "Analysis of broad-lined Type Ic supernovae from the (intermediate) Palomar Transient Factory". In: *Astronomy & Astrophysics* 621 (2019), A71. DOI: 10.1051/0004-6361/201834429.

[44] W. D. Arnett. "Type I supernovae. I - Analytic solutions for the early part of the light curve". In: *The Astrophysical Journal* 253 (1982), pp. 785–797. DOI: 10.1086/159681.

[45] N. Afsariardchi et al. "The Nickel Mass Distribution of Stripped-envelope Supernovae: Implications for Additional Power Sources". In: *The Astrophysical Journal* 918 (2021), p. 89. DOI: 10.3847/1538-4357/ac0aeb.

[46] A. H. Harutyunyan et al. "ESC supernova spectroscopy of non-ESC targets". In: *Astronomy and Astrophysics* 488.1 (2008), pp. 383–399. DOI: 10.1051/0004-6361:20078859.

[47] S. Blondin and J. L. Tonry. *SNID: Supernova Identification.* Astrophysics Source Code Library, record ascl:1107.001. 2011.

[48] N. Masetti et al. "Unveiling the nature of INTEGRAL objects through optical spectroscopy. V. Identification and properties of 21 southern hard X-ray sources". In: *Astronomy and Astrophysics* 459 (2006), pp. 21–30. DOI: 10.1051/0004-6361:20066055.

[49] *SN 2005gj.* https://www.wiserep.org/object/4791.

[50] J. L. Prieto et al. *A Study of the Type Ia/IIn Supernova 2005gj from X-ray to the Infrared: Paper I.* 2007. eprint: 0706.4088.

[51] *SN 2006aj.* https://www.wiserep.org/object/7999.

[52] P. Ferrero et al. "The GRB 060218/SN 2006aj event in the context of other gamma-ray burst supernovae". In: *Astronomy & Astrophysics* 457 (2006). DOI: 10.1051/0004-6361:20065530.

[53] *SN 2009ip.* https://www.wiserep.org/object/8993.

[54] R. Margutti et al. "A Panchromatic View of the Restless SN 2009ip Reveals the Explosive Ejection of a Massive Star Envelope". In: *The Astrophysical Journal* 780 (2014), p. 21. DOI: 10.1088/0004-637X/780/1/21.

[55] T.-W. Chen et al. "SN 2017ens: The Metamorphosis of a Luminous Broadlined Type Ic Supernova into an SN IIn". In: *The Astrophysical Journal* 867 (2018), p. L31. DOI: 10.3847/2041-8213/aaeb2e.

[56] R. A. Chevalier and C. Fransson. "Emission from Circumstellar Interaction in Normal Type II Supernovae". In: *Astrophysical Journal* 420 (1994), p. 268. DOI: 10.1086/173557.

[57]   B. Draine. "Physics of the Interstellar and Intergalactic Medium". In: *Physics of the Interstellar and Intergalactic Medium by Bruce T. Draine. Princeton University Press, 2011. ISBN: 978-0-691-12214-4* (2011), p. 143.

[58]   H. Karttunen, P. Kröger, H. Oja, M. Poutanen, and Karl Johan Donner. *Fundamental astronomy*. English. 5th ed. United States: Springer, 2007, pp. 243–261.

A Photometric data

Table X. Photometric data in the optical bands, *ugriz*-bands in AB system and *VB*-bands in Vega system.

Date (UT)	Telescope	MJD	u	B	g	V	r	i	z
2017-04-22	CSS	57865			18.95 ± 0.17	19.13 ± 0.13			
2017-04-28	CSS	57871			18.43 ± 0.13	18.91 ± 0.18			
2017-05-01	CSS	57874			18.19 ± 0.09	18.16 ± 0.09			
2017-05-02	LT+IO:O	57875			18.25 ± 0.11		17.97 ± 0.09	18.13 ± 0.04	18.13 ± 0.11
2017-05-03	LT+IO:O	57876	19.08 ± 0.06		18.33 ± 0.0		17.94 ± 0.0	18.1 ± 0.04	18.15 ± 0.12
2017-05-04	LT+IO:O	57877			18.35 ± 0.03		17.97 ± 0.05	18.08 ± 0.1	18.16 ± 0.06
2017-05-05	LT+IO:O	57878	19.82 ± 0.02		18.42 ± 0.02		17.97 ± 0.01	17.97 ± 0.01	18.07 ± 0.02
2017-05-08	LT+IO:O	57881			18.23 ± 0.01		17.85 ± 0.01	17.89 ± 0.01	17.9 ± 0.08
2017-05-12	LT+IO:O	57885			18.11 ± 0.08		17.81 ± 0.05	17.74 ± 0.04	17.74 ± 0.05
2017-05-13	LT+IO:O	57886			18.32 ± 0.29		17.98 ± 0.43	17.69 ± 0.67	
2017-05-14	LT+IO:O	57887	18.68 ± 0.03		18.08 ± 0.05		17.81 ± 0.08	17.72 ± 0.07	
2017-05-16	LT+IO:O	57889			17.97 ± 0.07		17.75 ± 0.12		
2017-05-17	LT+IO:O	57890			18.03 ± 0.11		17.74 ± 0.08	17.66 ± 0.07	17.64 ± 0.1
2017-05-21	LT+IO:O	57894			17.9 ± 0.03		17.69 ± 0.04	17.61 ± 0.08	17.56 ± 0.09
2017-05-21	LCOGT	57894			17.95 ± 0.04		17.62 ± 0.05	17.47 ± 0.08	
2017-05-24	LT+IO:O	57897			17.7 ± 0.09		17.57 ± 0.06	17.48 ± 0.1	17.47 ± 0.12
2017-05-26	NOT+ALFOSC	57899	18.94 ± 0.06	17.82 ± 0.00	17.64 ± 0.01	17.48 ± 0.00	17.52 ± 0.01	17.42 ± 0.01	17.36 ±0.01
2017-05-30	LT+IO:O	57903			17.51 ± 0.00		17.37 ± 0.00	17.36 ± 0.00	17.24 ± 0.01

Table XI. Photometric data in the optical bands, *ugriz*-bands in AB system and *VB*-bands in Vega system.

Date (UT)	Telescope	MJD	u	B	g	V	r	i	z
2017-05-31	LT+IO:O	57904			17.41 ± 0.07		17.39 ± 0.06	17.4 ± 0.07	17.31 ± 0.09
2017-06-10	LT+IO:O	57914	17.90 ± 0.08		17.29 ± 0,08		17.24 ± 0.05	17.21 ± 0.05	
2017-06-11	LT+IO:O	57915			17.25 ± 0.04		17.24 ± 0.04	17.27 ± 0.07	
2017-06-14	LT+IO:O	57918			17.2 ± 0.06		17.23 ± 0.06	17.28 ± 0.06	17.09 ± 0.05
2017-06-24	LCOGT	57928			17.26 ± 0.03		17.17 ± 0.03	17.21 ± 0.03	
2017-06-28	NOT+ALFOSC	57932	17.77 ± 0.08	17.43 ± 0.00	17.2 ± 0.02	17.09 ± 0.00	17.21 ± 0.01	17.23 ± 0.01	17.05 ± 0.02
2017-07-02	CSS	57936				17.10 ± 0.00			
2017-07-13	LCOGT	57948			17.29 ± 0.03		17.21 ± 0.04	17.34 ± 0.03	
2017-07-22	NOT+ALFOSC	57956	18.01 ± 0.13	17.51 ± 0.01	17.29 ± 0.02	17.15 ± 0.01	17.26 ± 0.01	17.36 ± 0.01	16.96 ± 0.03
2017-10-22	NOT+ALFOSC	58048		18.39 ± 0.01		18.07 ± 0.00	17.94 ± 0.01	18.48 ± 0.0	17.25 ± 0.19
2017-10-27	LT+IO:O	58053		18.52 ± 0.22	18.28 ± 0.15	18.03 ± 0.13	18.12 ± 0.21	18.35 ± 0.19	17.71 ± 0.23
2017-11-01	LT+IO:O	58058		18.55 ± 0.05	18.21 ± 0.04	18.18 ± 0.05	18.1 ± 0.07	18.47 ± 0.08	17.71 ± 0.07
2017-11-12	LT+IO:O	58069		18.80 ± 0.09	18.46 ± 0.13	18.03 ± 0.12	18.51 ± 0.29	18.82 ± 0.24	17.58 ± 0.6
2017-11-15	LT+IO:O	58072			18.55 ± 0.08		18.37 ± 0.08	18.75 ± 0.08	18.0 ± 0.1
2017-11-18	LT+IO:O	58075		18.88 ± 0.06	18.57 ± 0.0	18.53 ± 0.03	18.47 ± 0.03	18.81 ± 0.02	18.04 ± 0.03
2017-11-21	LT+IO:O	58078			18.63 ± 0.17		18.51 ± 0.15	18.59 ± 0.25	18.04 ± 0.47
2017-11-24	LT+IO:O	58081			18.69 ± 0.07		18.51 ± 0.07	19.03 ± 0.15	18.19 ± 0.16
2017-12-24	CSS	58101				18.74 ± 0.12			
2017-12-15	LT+IO:O	58102			19.21 ± 0.08		19.04 ± 0.07	19.29 ± 0.12	18.64 ± 0.12

Table XII. Photometric data in the optical bands, *ugriz*-bands in AB system and *VB*-bands in Vega system.

Date (UT)	Telescope	MJD	u	B	g	V	r	i	z
2017-12-18	LT+IO:O	58105			19.24 ± 0.09		19.08 ± 0.11	19.49 ± 0.18	18.53 ± 0.12
2017-12-20	LT+IO:O	58107		19.58 ± 0.07	19.34 ± 0.05	19.32 ± 0.05	19.11 ± 0.05	19.5 ± 0.12	18.7 ± 0.08
2017-12-21	LT+IO:O	58108			19.38 ± 0.06		19.17 ± 0.07	19.48 ± 0.1	18.8 ± 0.11
2017-12-21	CSS	58108				18.82 ± 0.02			
2017-12-25	LT+IO:O	58112			19.45 ± 0.04		19.26 ± 0.06	19.56 ± 0.1	18.85 ± 0.11
2017-12-25	CSS	58112				18.96 ± 0.12			
2017-12-26	LT+IO:O	58113			19.49 ± 0.04		19.29 ± 0.05	19.64 ± 0.14	18.87 ± 0.09
2017-12-28	LT+IO:O	58115			19.58 ± 0.02		19.35 ± 0.02	19.66 ± 0.01	18.96 ± 0.01
2017-12-29	LT+IO:O	58116			19.56 ± 0.08		19.32 ± 0.05	19.64 ± 0.1	18.97 ± 0.09
2018-01-01	LT+IO:O	58119			19.42 ± 0.2		19.25 ± 0.14	19.63 ± 0.15	19.0 ± 0.15
2018-01-11	LT+IO:O	58129			19.94 ± 0.06		19.69 ± 0.07	20.0 ± 0.1	19.28 ± 0.12
2018-01-12	CSS	58130				19.28 ± 0.14			
2018-01-15	CSS	58133				19.38 ± 0.15			
2018-01-18	CSS	58136				19.52 ± 0.16			
2018-01-20	LT+IO:O	58138			20.13 ± 0.07		19.67 ± 0.09	19.93 ± 0.11	19.41 ± 0.15
2018-01-22	LT+IO:O	58140			19.94 ± 0.06		19.64 ± 0.09	20.02 ± 0.15	19.35 ± 0.2
2018-01-23	CSS	58141				19.76 ± 0.17			
2018-01-28	LT+IO:O	58146			20.15 ± 0.21		19.9 ± 0.18	20.19 ± 0.29	19.6 ± 0.2
2018-02-14	NOT+ALFOSC	58163			20.71 ± 0.0		19.69 ± 0.52		
2018-04-11	NOT+ALFOSC	58219			21.36 ± 0.04		20.19 ± 0.58		
2018-05-19	NOT+ALFOSC	58257			21.41 ± 0.02		20.36 ± 0.55	20.84 ± 0.02	20.83 ± 0.02

Table XIII. Photometric data taken with ATLAS in orange (o) and cyan (c) bands, both in AB system.

Date (UT)	MJD	o	c
2017-04-20	57863	19.05 ± 0.29	
2017-04-25	57868	18.48 ± 0.17	
2017-04-26	57869		18.37 ± 0.05
2017-05-07	57880	18.05 ± 0.1	
2017-05-08	57881	17.98 ± 0.05	
2017-05-09	57882	17.94 ± 0.09	
2017-05-12	57885	17.63 ± 0.06	
2017-05-14	57887	17.82 ± 0.04	
2017-05-16	57889	17.92 ± 0.04	
2017-05-18	57891	17.86 ± 0.04	
2017-05-20	57893		17.97 ± 0.03
2017-05-23	57896	17.69 ± 0.04	
2017-05-26	57899	17.6 ± 0.02	
2017-05-27	57900	17.58 ± 0.03	
2017-05-28	57901		17.62 ± 0.02
2017-05-30	57903	17.5 ± 0.03	
2017-06-03	57907	17.45 ± 0.05	
2017-06-05	57909	17.48 ± 0.05	
2017-06-09	57913	17.37 ± 0.07	
2017-06-20	57924	17.26 ± 0.02	
2017-06-24	57928	17.25 ± 0.02	
2017-06-28	57932	17.26 ± 0.02	
2017-07-02	57936	17.29 ± 0.02	
2017-07-06	57940	17.33 ± 0.03	
2017-07-08	57942	17.28 ± 0.04	
2017-07-12	57946	17.31 ± 0.03	
2017-07-14	57948	17.34 ± 0.04	
2017-10-29	58055	18.52 ± 0.08	
2017-11-02	58059	18.53 ± 0.1	
2017-11-06	58063	18.57 ± 0.2	
2017-11-08	58065	18.64 ± 0.16	
2017-12-14	58101	19.63 ± 0.13	
2017-12-18	58105	19.8 ± 0.21	

Table XIV. Photometric NIR data in the Vega system.

Date (UT)	Telescope	MJD	J	H	K
2017-07-27	NOT+NOTCAM	57961	16.93 ± 0.01	16.50 ± 0.01	16.24 ± 0.01
2017-07-28	NOT+NOTCAM	57962	16.95 ± 0.02	16.51 ± 0.03	16.23 ± 0.05
2018-01-22	NOT+NOTCAM	58140	17.58 ± 0.01	16.38 ± 0.01	15.34 ± 0.01
2018-01-23	NOT+NOTCAM	58141	17.53 ± 0.05	16.18 ± 0.25	15.19 ± 0.25
2018-03-31	NOT+NOTCAM	58208	18.43 ± 0.01	16.94 ± 0.01	15.77 ± 0.01
2018-06-10	NOT+NOTCAM	58279	19.23 ± 0.11	17.48 ± 0.35	16.14 ± 0.24